Barotropic and Baroclinic Eddy Feedbacks in the Midlatitude Jet Variability and Responses to Climate Change–Like Thermal Forcings

D. Alex Burrows

Department of Earth and Atmospheric Sciences, Cornell University, Ithaca, New York

Gang Chen

Department of Earth and Atmospheric Sciences, Cornell University, Ithaca, New York, and Department of Atmospheric and Oceanic Sciences, University of California, Los Angeles, Los Angeles, California

Lantao Sun

Cooperative Institute for Research in Environmental Sciences, University of Colorado Boulder, and NOAA/Earth System Research Laboratory, Boulder, Colorado

(Manuscript received 5 February 2016, in final form 23 September 2016)

ABSTRACT

Studies have suggested that the persistence in the meridional vacillation of the midlatitude jet (i.e., annular mode time scale) in comprehensive climate models is related to the model biases in climatological jet latitude, with important implications for projections of future climates and midlatitude weather events. Through the use of the recently developed finite-amplitude wave activity formalism and feedback quantifying techniques, this paper has quantified the role of barotropic and baroclinic eddy feedbacks in annular mode time scales using an idealized dry atmospheric model.

The eddy–mean flow interaction that characterizes the persistent anomalous state of the midlatitude jet depends on processes associated with the lower-tropospheric source of vertically propagating Rossby waves, baroclinic mechanisms, and processes associated with upper-tropospheric wave propagation and breaking, barotropic mechanisms. A variety of climate change–like thermal forcings are used to generate a range of meridional shifts in the midlatitude eddy-driven jet. The idealized model shows a reduction in annular mode time scale associated with an increase in jet latitude, similar to comprehensive climate models. This decrease in time scale can be attributed to a similar decrease in the strength of the barotropic eddy feedback, which, in the positive phase of the annular mode, is characterized by anomalous potential vorticity (PV) mixing on the equatorward flank of the climatological jet. The decrease in subtropical PV mixing is, in turn, associated with a stronger subtropical jet as the eddy-driven jet is more distant from the subtropics. These results highlight the importance of subtropical eddy–mean flow interactions for the persistence of an eddy-driven jet.

1. Introduction

The meridional vacillation of the midlatitude jet about its climatological position, known as the zonal index or annular mode (e.g., Thompson and Wallace 2000), describes the leading mode of extratropical atmospheric variability. The zonal jet vacillation and its associated eddy feedback are important for stratosphere–troposphere coupling and tropospheric predictability (Baldwin and Dunkerton 2001; Garfinkel et al. 2013), tropospheric blocking patterns (Woollings and Hoskins 2008), Rossby wave breaking (e.g., Benedict et al. 2004; Franzke et al. 2004; Strong and Magnusdottir 2008), and the extratropical circulation responses to El Niño (L'Heureux and Thompson 2006; Chen and Zurita-Gotor 2008) and ozone depletion (e.g., Gillett and Thompson 2003; Son et al. 2009; Perlwitz et al. 2008). More recently, there are conflicting viewpoints with respect to the response of midlatitude jet stream structures and extreme weather events to Arctic warming [see Hoskins and Woollings (2015) and references therein]. Therefore, an understanding of midlatitude jet dynamics is essential for the extratropical atmospheric variability from intraseasonal to decadal time scales.

Corresponding author e-mail: D. Alex Burrows, db647@cornell.edu

The zonal jet vacillation can be simulated in a wide variety of models from quasigeostrophic models (Lee and Feldstein 1996; Zhang et al. 2012) to idealized primitive equation models (Gerber and Vallis 2007; Chen and Plumb 2009) to comprehensive general circulation models (Gerber et al. 2008a; Barnes and Hartmann 2010). While the meridional shift in zonal wind can be interpreted as a consequence of the conservation of angular momentum (Gerber and Vallis 2005), the time scale associated with the jet shift is more complicated and warrants further inspection because of its implication for predictability and climate sensitivity (Gerber et al. 2008b). The annular mode is well described by the vertical- and zonal-mean zonal wind that is driven by eddy momentum forcing and damped by friction (Chen and Plumb 2009), and the associated eddies contain power in short time scales that rapidly initiates an annular mode response and power at longer time scales that maintains a shifted jet (Lorenz and Hartmann 2001). This low-frequency pumping of the eddy momentum flux sustains a zonal wind anomaly against frictional damping, and this contributes to the persistent zonal wind anomaly associated with the annular modes (Feldstein and Lee 1998; Robinson 2000; Gerber and Vallis 2007; Hartmann 2007; Lorenz 2014).

Debate continues as to how to quantify the mechanisms, barotropic or baroclinic, responsible for the annular mode persistence. Variations in baroclinic eddy generation in the lower troposphere, which provide upward wave activity fluxes, have been presented to explain annular mode persistence. In observations, Lorenz and Hartmann (2001) showed that accompanying the zonal wind anomaly is a similar shift in the maximum low-level baroclinicity, providing a baroclinic feedback. This may be attributed to an indirect residual meridional circulation induced by a wave activity flux convergence at the jet core (Robinson 2006; Gerber and Vallis 2007) or the direct heat transport by low-frequency eddies (Zhang et al. 2012). Surface friction, which induces a low-level vertical shear in zonal wind through thermal wind considerations, helps to maintain a baroclinic mechanism (Robinson 2000; Chen and Plumb 2009). However, even in a stirred barotropic model with the latitude of stirring fixed, positive eddy feedbacks can be obtained, indicating mechanisms other than baroclinic feedback at play (Vallis et al. 2004; Barnes et al. 2010; Barnes and Hartmann 2011; Lorenz 2014).

The meridional wave propagation in the upper troposphere (or in a barotropic model) can result in growing waves near the critical latitudes that often lead to wave breaking and irreversible potential vorticity (PV) mixing. Waves tilt in the northeast–southwest
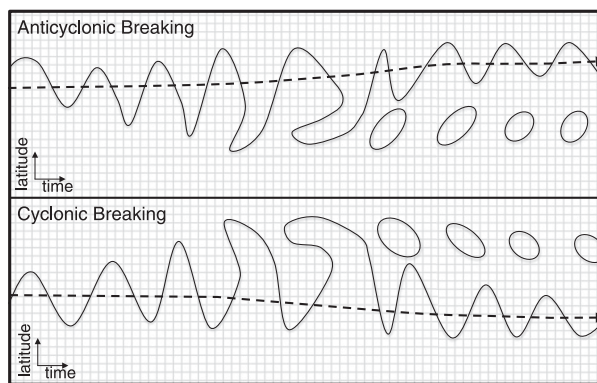

FIG. 1. Schematic indicating the direction of wave propagation that is consistent with the (top) positive and (bottom) negative phase of the annular mode as a function of time and latitude associated with anticyclonic and cyclonic wave breaking, respectively. Solid lines represent PV contours, and the dashed line represents the jet latitude.

direction and predominantly break anticyclonic on the equatorward flank of the climatological jet leading to poleward momentum fluxes that shift the jet (see Fig. 1). The opposite can be stated for northwest–southeast-tilting, cyclonic breaking waves with equatorward momentum fluxes. These wave breaking characteristics coincide strongly with the zonal wind anomalies associated with the annular modes (Benedict et al. 2004; Franzke et al. 2004; Strong and Magnusdottir 2008; Nie et al. 2014). Although much insight in wave propagation has been gained using linear wave theory (e.g., Simmons and Hoskins 1978; Hartmann and Zuercher 1998; Chen and Zurita-Gotor 2008; Lorenz 2014), the irreversible characteristics of Rossby wave breaking present many difficulties in quantifying the eddy–zonal flow interactions that are evident in interacting positive and negative feedbacks (e.g., Zurita-Gotor et al. 2014).

The finite-amplitude wave activity formalism from Nakamura and Zhu (2010) provides a mathematically rigorous framework to quantify the effect of wave breaking on the zonal flow. More specifically, these regions of wave breaking and eddy mixing can be described by large values of effective diffusivity where PV contours have been stretched from zonal symmetry. This formalism has a direct connection to the well-known nonacceleration theorem: that is, for a conservative flow in the steady state, the eddies can neither accelerate nor decelerate the zonal jet [see section 7.4 of Vallis (2006)]. As such, Chen et al. (2013) showed the eddy momentum forcing associated with meridional wave propagation can be decomposed into transient wave activity, (baroclinic) vertical wave propagation, and (barotropic) nonconservative PV mixing. Nie et al. (2014) further applied this decomposition to the Southern Hemisphere

annular mode (SAM) and demonstrated that the positive eddy feedback in the annular mode can be attributed to both barotropic and baroclinic mechanisms.

More importantly, the eddy feedbacks are salient for understanding the relationship between the biases in climatological jet latitude and the circulation responses to climate change. Comprehensive climate models with biases in SH climatological jet latitude (e.g., Fyfe and Saenko 2006; Swart and Fyfe 2011, 2012), specifically equatorward biases, are shown to exhibit time scales of variability in the annular mode beyond what is observed (Gerber et al. 2008b; Kidston and Gerber 2010; Barnes and Hartmann 2010) and display greater sensitivity in climate projections, such as increased CO_2 (Woollings et al. 2010; Arakelian and Codron 2012), in accordance with fluctuation–dissipation theorem (Leith 1975; Ring and Plumb 2008). Although it has been recognized that a subtropical jet can interact with an eddy-driven jet so as to impact the unforced variability of the eddy-driven jet (Eichelberger and Hartmann 2007; Barnes and Hartmann 2011), Barnes et al. (2010) explained the impact of jet latitude on the annular mode time scale by the change in wave breaking on the jet's poleward flank. However, using a bias correction technique, Simpson et al. (2013) showed evidence that correcting the mean jet latitude does not improve the model biases in the annular mode time scale, and therefore additional investigation is warranted on the dynamics of eddy feedback.

This study investigates the dynamics of eddy feedback in jet variability by employing the Geophysical Fluid Dynamics Laboratory (GFDL) atmospheric dynamical core. Through the use of lagged-covariance analysis and the finite-amplitude wave activity formalism, we first demonstrate that barotropic and baroclinic feedbacks in the annular mode variability can be quantified as in Nie et al. (2014) and that both baroclinic and barotropic feedbacks act to extend the persistence of a zonal wind anomaly. Next, perturbations are used to mimic climate responses, such as tropical temperature warming analogous to El Niño–Southern Oscillation, tropical upper warming analogous to greenhouse gas warming, and Arctic surface warming/cooling analogous to Arctic amplification (e.g., Butler et al. 2010; Sun et al. 2013; Lu et al. 2014), and these perturbations allow us to investigate how the feedback strengths vary when the climatological jet latitude is varied. In agreement with Simpson et al. (2012), who found the reduction in eddy feedback with increasing jet latitude to depend on the equatorward flank of the climatological jet through subtropical, eddy–mean flow interaction, it is found that, with an increase in jet latitude, the annular mode time scale and the strength of the eddy feedbacks decrease,

with the dominant contribution from the barotropic feedback characterized by a reduction in anomalous effective diffusivity in the subtropics.

The paper is organized as follows. Section 2 outlines the model employed along with details of the thermal perturbations used to create various experiments with different climatological jet latitudes. Section 3 will describe the wave activity diagnostics and quantification of feedback strength used in this study through the use of the control run. This will be followed by a discussion of the spatial and temporal characteristics of annular mode variability identified under idealized climate change along with a discussion of the effect of feedback strength on the annular mode time scale in section 4. Section 5 compares the wave activity analysis with previous studies using linear theory of Rossby wave propagation. A conclusions section will finish the paper.

2. Model setup and idealized thermal forcings

The model used is the GFDL dry atmospheric dynamical core. The control simulation follows the configuration described in Held and Suarez (1994), which is driven by a relaxation toward a zonally symmetric radiative-equilibrium temperature profile and damped by linear friction in the planetary boundary layer. Idealized thermal perturbations are utilized as a means of systematically shifting the climatological jet, either equatorward or poleward of the control run. Most of the simulations are performed at a rhomboidal 30 (R30) spectral harmonic truncation with 20 evenly spaced sigma levels. Eighth-order horizontal hyperdiffusion is used with a damping time scale of 0.1 day for the smallest resolved scales in the model. Each model configuration is integrated for 12 000 days using the last 11 500 days after spinup. All of the results presented in the paper are qualitatively unchanged when using half the data. Furthermore, selected simulations are conducted at a higher horizontal resolution (R60) and at triangular spectral truncations (T42 and T85) to confirm the robustness of these results. All the model simulations are summarized in Table 1.

More specifically, the radiative-equilibrium-temperature profile is given as

$$T_{eq} = \max\left\{200, \left[315 - \delta_y \sin^2\phi - \delta_y F(p)W(\phi, \phi_0)\right.\right.$$
$$\left.\left. - \delta_z \log\left(\frac{p}{p_0}\right)\cos^2\phi\right]\left(\frac{p}{p_0}\right)^\kappa\right\}, \quad (1)$$

where ϕ is latitude, p is pressure, $p_0 = 1000$ hPa, $\delta_y = 60$ K, and $\delta_z = 10$ K. The $F(p)$ and $W(\phi, \phi_0)$ are functions to be defined below. For the control run simulation, $F(p)$

TABLE 1. A list of the numerical values used in the thermal perturbation runs. For the TTW and TUW runs, the parameters in Eq. (1) are altered: $F(p)$ and $W(\phi, \phi_0)$ set the vertical and meridional structure of the heating, where ϕ_0 is the latitudinal width of the warming perturbation, and $\delta\phi = 5°$ sets the meridional sharpness of the thermal perturbation boundary. For the ASW/C runs, an additional heating rate is specified by $\partial T/\partial t|_{\text{ASW/C}}$ with $F(p) = 0$. For all the runs, A_0 is the magnitude of the heating, and p_0 is 1000 hPa. Notice the ASW runs have positive A_0, and ASC runs have negative values. All the simulations are run at the R30 resolution, and the bold letters in the TTW section indicate the simulations conducted at R60, T42, and T85 resolutions.

Experiment description	ϕ_0	A_0
TTW	10°, 30°	−0.015 625
$F(p) = A_0$	10°, 30°	−0.031 25
$W(\phi, \phi_0) = 0.5\{1 - \tanh[(|\phi| - \phi_0)/\delta\phi]\}$	**10°, 30°**	**−0.0625**
	10°, 30°	−0.125
	10°, 30°	**−0.25**
TUW	10°, 30°	−0.015 625
$F(p) = A_0 \exp[-(p/p_0 - 0.3)^2/(2 \times 0.11^2)]$	10°, 30°	−0.031 25
$W(\phi, \phi_0) = 0.5\{1 - \tanh[(|\phi| - \phi_0)/\delta\phi]\}$	10°, 30°	−0.0625
	10°, 30°	−0.125
	10°, 30°	−0.25
ASW/C	—	0.125/−0.125
$\left.\dfrac{\partial T}{\partial t}\right|_{\text{ASW/C}} = A_0 \cos^{15}(\phi - \pi/2) \exp\left[6\left(\dfrac{p}{p_0} - 1\right)\right], \quad (\phi > 0)$	—	0.25/−0.25
$F(p) = 0$	—	0.5/−0.5
	—	1.0/−1.0
	—	2.0/−2.0

in Eq. (1) is set to zero as the standard Held and Suarez (1994) configuration. Three types of thermal perturbations are examined and outlined below, including tropical tropospheric warming, tropical upper-tropospheric warming and, Arctic surface warming–cooling (Butler et al. 2010; Sun et al. 2013). The first two perturbations are imposed by altering the parameters in radiative-equilibrium temperature T_{eq}, and the third one is introduced by an additional heating rate $\partial T/\partial t|_{\text{ASW/C}}$ where the ASW/C stands for Arctic surface warming/cooling. As a note, the direct effect of introducing temperature perturbations does not affect the midlatitude PV structure and the jet latitude, while the indirect effect induced by the general circulation and eddies does alter the PV structure that the jet stream does adjust to.

a. Tropical tropospheric warming (TTW)

The functions of $F(p)$ and $W(\phi, \phi_0)$ in T_{eq} are designed to increase the radiative-equilibrium temperature of Held and Suarez (1994) in the tropical troposphere without altering the stratospheric temperature. Particularly, $F(p)$ defines the vertical structure of the thermal perturbation, and $W(\phi, \phi_0) = 0.5\{1 - \tanh[(|\phi| - \phi_0)/\delta\phi]\}$ is a weighting function that sets the meridional structure, with ϕ_0 setting the boundary of the warming and $\delta\phi = 5°$ setting the sharpness of the boundary. A narrow warming with $\phi_0 = 10°$ and a broad warming with $\phi_0 = 30°$ are used and will be shown below.

The tropical tropospheric warming (TTW) runs specify a heating profile that is independent of height in the troposphere [i.e., $F(p) = A_0$ in Eq. (1)], and thus it produces a warming throughout the depth of the troposphere. Figures 2a and 2b show an example of both narrow and broad warming compared with the control run. These two examples have used the quadrupled parameter of $A_0 = -0.25$ with the radiative-equilibrium-temperature profile change indicated by green contours, see details of A_0 below. The prescribed radiative-equilibrium temperature change produces local warming plus an indirect remote temperature change associated with the change in dynamics. The climatological zonal wind response, indicated by black contours, is an equatorward shift for narrow warming and a poleward shift for broad warming. The opposite shifts in jet latitude from the TTW cases can be understood as a tug of war between the equatorward shift of the low-level baroclinicity and the increased subtropical wave breaking, both of which can alter and shift the eddy momentum flux in the upper troposphere (Sun et al. 2013). A secondary increase in zonal wind is discerned in the tropics for narrow warming and subtropical regions for broad warming.

To produce experiments with a systematic shift in jet latitude, the magnitude of the heating is altered for both narrow and broad experiments. This is done by quartering, halving, doubling, and quadrupling the standard perturbation runs described above (i.e., $A_0 = -0.0625$). Runs are performed with $A_0 = -0.015\,625$ for the quarter run, $A_0 = -0.031\,25$ for the half run, $A_0 = -0.125$ for the double run, and $A_0 = -0.25$ for the quadruple run. This produces 10 experiments with jet
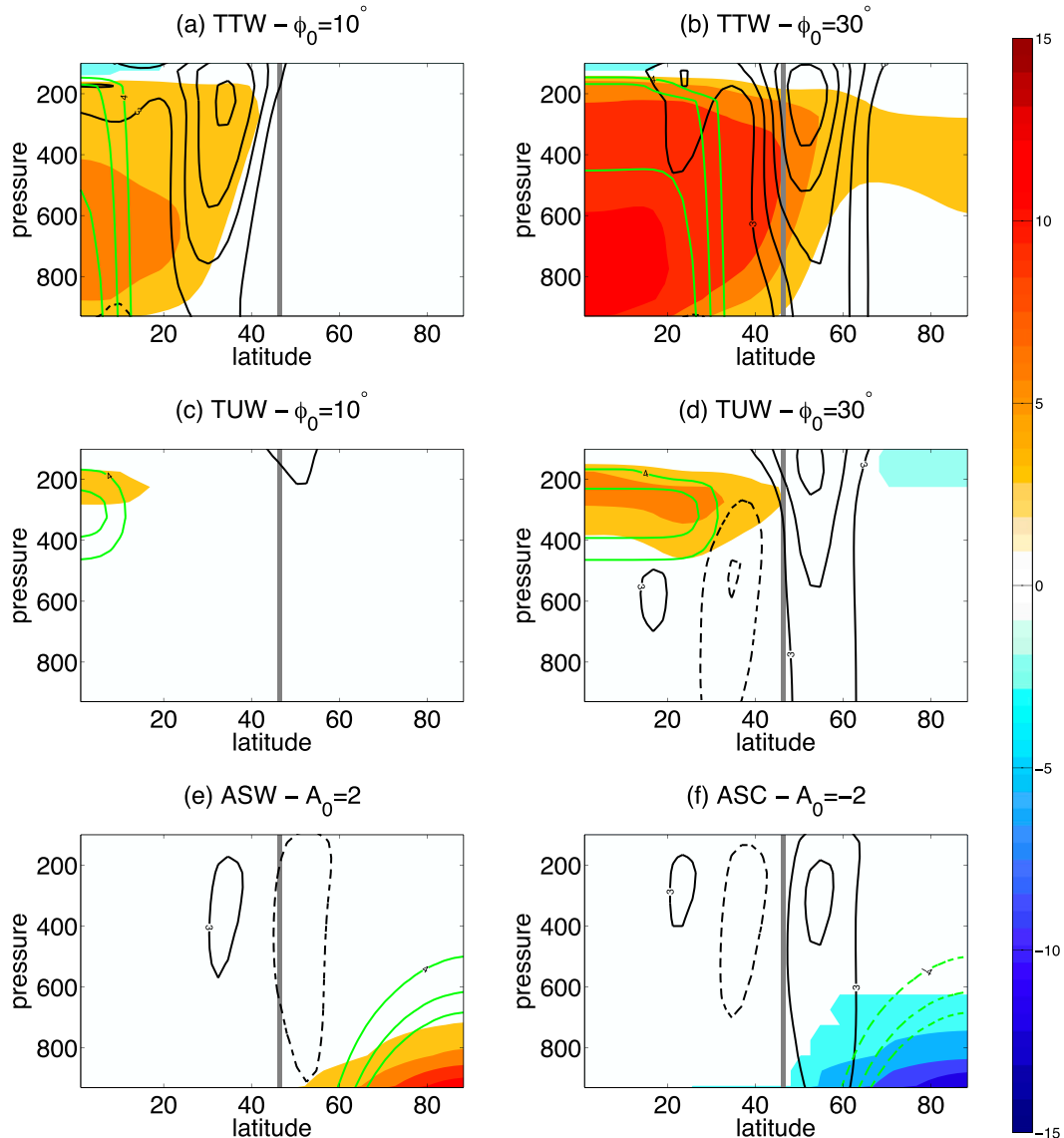
FIG. 2. Responses in radiative-equilibrium-temperature profiles (green contours with 4-, 8-, and 12-K contours), actual temperature (color shades with a 3-K interval) and zonal-mean zonal wind (m s^{-1}; black contours) between forced runs and the control run for (a),(b) TTW runs, (c),(d) TUW runs, and (e),(f) ASW/C runs. For the TTW and TUW runs, (left) 10° wide runs and (right) 30° wide runs are given. For the ASW/C runs, (left) warming and (right) cooling are shown. Dashed contours are negative, and the vertical gray line in each plot indicates the climatological jet latitude for the control run. Each forced run uses the quadrupled value of A_0, which shows the biggest forced response.

latitudes ranging from about 40° to 50°. Although the eddy-driven jet does not reach latitudes as far poleward as the SH eddy-driven jet (e.g., about 52°), these model settings were used to obtain a variety of possible jet latitudes to analyze eddy–mean flow feedbacks.

b. TUW

A tropical upper-tropospheric warming (TUW) signature (Sun et al. 2013) is produced by using $F(p) = A_0 \exp[-(p/p_0 - 0.3)^2/(2 \times 0.11^2)]$ in Eq. (1),

which sets the vertical extent of the warming similar to Butler et al. (2010). Figures 2c and 2d show the spatial structure of the response in radiative equilibrium and actual temperatures again for the narrow and broad warming scenarios for the quadruple forced runs. In contrast to the TTW runs, the response of the climatological zonal wind is a poleward shift for both narrow and broad warmings compared to the control run. The zonal wind shift is much smaller and weaker for the narrow warming. Sun et al. (2013) showed that the shift
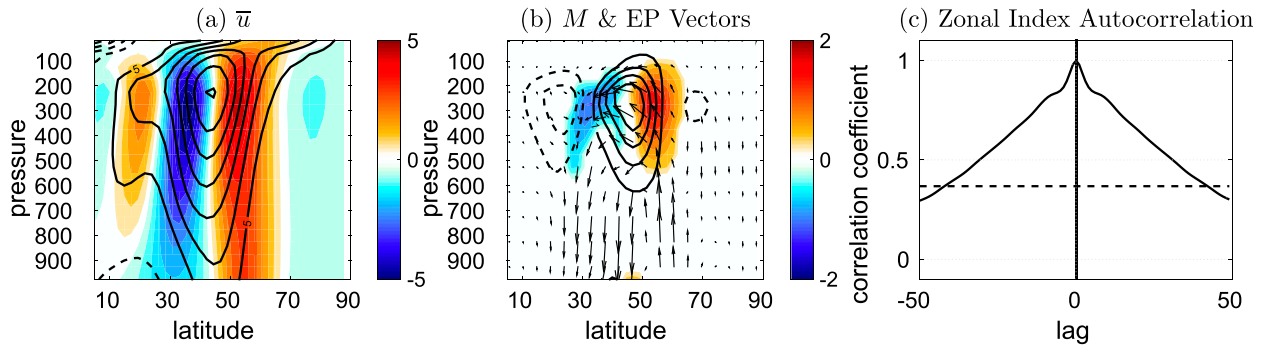
FIG. 3. Control run climatology (contours) and lag 0 regressions onto the zonal index (color shading), representing the leading mode of variability, for (a) zonal-mean zonal wind and (b) eddy momentum flux convergence and Eliassen–Palm vectors. Negative contours are dashed. The contour interval for the regression in (a) is 0.5 m s^{-1} and in (b) is 0.2 m s^{-2}. (c) Lagged autocorrelation of the zonal index. The horizontal dashed line is the value of the e-folding time scale.

in zonal wind for a broad warming can be explained by an increase in effective diffusivity associated with enhanced irreversible PV mixing in the subtropics, consistent with poleward shifts in both cyclonic and anticyclonic wave breaking for the broad warming scenario (Lu et al. 2014) and poleward-shifted eddy momentum forcing. As for the TTW runs, the magnitude of the heating is altered by quartering, halving, doubling, and quadrupling the standard perturbation runs for both narrow and broad experiments, and thus a range of changes in jet latitude are produced.

c. ASW/C

An Arctic amplification-like signature is generated by using a thermal forcing from Butler et al. (2010). Rather than altering the T_{eq} profile, the thermal forcing is applied to the Northern Hemisphere by prescribing the additional heating rate as

$$\left.\frac{\partial T}{\partial t}\right|_{\text{ASW/C}} = A_0 \cos^{15}(\phi - \pi/2) \exp\left[6\left(\frac{p}{p_0} - 1\right)\right], \quad (\phi > 0),$$
(2)

with $p_0 = 1000 \text{ hPa}$. The equivalent change in T_{eq} can be inferred by multiplying the heating rate with the radiative relaxation time scale. Figures 2e and 2f show the corresponding structure of the changes in radiative-equilibrium temperature, actual temperature, and zonal wind response. As in Butler et al. (2010), a low-level warming in the Arctic shifts the jet equatorward, and, conversely, cooling in the Arctic shifts the jet poleward. Similar to the TTW and TUW runs, five magnitudes of Arctic surface warming (ASW) are applied, including $A_0 = 0.125$ for the quarter run, $A_0 = 0.25$ for the half run, $A_0 = 0.5$ for the standard run, $A_0 = 1$ for the double run, and $A_0 = 2$ for the quadruple run. Also, five Arctic surface cooling (ASC) runs are conducted by

reversing the sign of A_0, which produces jet shifts in the opposite direction. This leads to 10 ASW/C runs. In all the simulations considered here, TTW, TUW, and ASW/C runs, the climatological jet system is characterized by a blurred subtropical and eddy-driven jet except for the most equatorward jets that merge the two jet systems together.

3. Annular mode time scale and feedbacks in the control run

This section will provide details of the diagnostics used in this study through analyzing the annular mode time scale and associated eddy feedback in the control run.

a. Annular mode time scale

As is common in annular mode variability analyses, the principal component time series of the vertical- and zonal-mean zonal wind in the extratropics (between 20° and 70° latitude), weighted by $(\cos\phi)^{1/2}$, following Baldwin et al. (2009), will be used to describe the meridional departure of the midlatitude jet stream from climatology and is referred to as z, the zonal index. The associated empirical orthogonal function (**E**) structure, in meters per second, is demonstrated in Fig. 3 as a regression onto the standardized z values. As in the SH observations (Lorenz and Hartmann 2001), the poleward shift of the jet in the positive phase of the annular mode is associated with a similar poleward shift in the eddy momentum flux convergence. The low-level baroclinic source also shifts poleward in association with the poleward jet shift. As reviewed in the introduction, previous studies have attributed either the upper-level wave propagation and wave breaking or the lower-level baroclinic source to the poleward jet shift in the SH as well as the extended persistence of the anomalous

zonal wind (e.g., Lorenz and Hartmann 2001; Nie et al. 2014).

This persistence in zonal wind is highlighted with the autocorrelation of z to describe the temporal aspects of annular mode variability. Observations show an intraseasonal variability of the e-folding time scales ranging from about 6 to 20 days in the troposphere for both the NH and SH (Baldwin et al. 2003). With regard to the Held and Suarez (1994) system, Gerber et al. (2008b) found the annular mode time scale converges to 20–25 days at sufficiently high horizontal and vertical resolutions. In our control run, the e-folding time scale is about 43 days, as indicated by the horizontal dashed line in Fig. 3c. This large annular mode time scale can be attributed to the coarse R30 resolution, as found in Gerber et al. (2008b). Sun et al. (2013) found that the responses of zonal wind to idealized thermal perturbations are qualitatively similar at higher resolutions, although the magnitude of the responses in zonal wind is smaller, as expected from the fluctuation-dissipation theorem (Ring and Plumb 2008; Gerber et al. 2008b), because of the change in annular mode time scales with resolution. Given the qualitatively similar results at high resolutions, here we focus on the R30 simulations that can be used to explore a wide range in the model parameter space. Selected simulations are verified at R60, T42, and T85 resolutions (see Table 1 and Fig. 9).

b. Finite-amplitude wave activity

It is well recognized that the vertically and zonally averaged zonal wind is driven by eddy momentum flux convergence M against the surface friction F_r (e.g., Lorenz and Hartmann 2001):

$$\frac{\partial \langle \overline{u} \rangle}{\partial t} = \langle M \rangle - \langle \overline{F_r} \rangle, \tag{3}$$

where $M \equiv -1/(a \cos^2\phi)\partial(\overline{v'u'} \cos^2\phi)/\partial\phi$ and a is Earth's radius. Overbars and primes denote zonal means and deviations from zonal mean, respectively. The vertical average of X is denoted as $\langle X \rangle = (1/p_s)\int_0^{p_s} X\, dp$, where p_s is the surface pressure.

To understand the eddy momentum forcing, we use the finite-amplitude wave activity framework introduced by Nakamura and Zhu (2010). The waviness of quasigeostrophic PV contours is defined as

$$A = \frac{1}{2\pi a \cos\phi_e}$$
$$\times \left(\iint_{q_g>Q,\phi\leq\phi_e(Q)} q_g\, d\mathbf{S} - \iint_{q_g\leq Q,\phi>\phi_e(Q)} q_g\, d\mathbf{S} \right), \tag{4}$$

where A is the wave activity and $d\mathbf{S} = a^2 \cos\phi\, d\lambda\, d\phi$. The equivalent latitude ϕ_e corresponds to the PV contour $q_g = Q$ such that the area enclosed by the Q contour toward the North Pole is equal to the area enclosed poleward of ϕ_e (Butchart and Remsberg 1986). A physical interpretation of wave activity is to consider a PV field that is zonally symmetric and increasing toward the pole, which would provide a wave activity of zero, whereas PV contours with excessive north–south undulations provide a positive definite quantity of wave amplitude, where larger wave amplitudes correspond to larger values of A.

Following Chen et al. (2013), the eddy momentum flux convergence can be approximately decomposed into three components:

$$M = -f\frac{\partial}{\partial p}\left(\frac{\overline{v'\theta'}}{\overline{\theta}_p}\right) - \frac{\kappa_{\text{eff}}}{a}\frac{\partial Q}{\partial \phi_e} - \frac{\partial A}{\partial t}. \tag{5}$$

Here, $f = 2\Omega \sin\phi$ denotes planetary vorticity. The first term on the right-hand side (RHS) is the vertical convergence of wave activity flux from the low-level baroclinic eddy generation (Edmon et al. 1980). The second term is the effective diffusivity κ_{eff} multiplied by the meridional Lagrangian PV gradient. The effective diffusivity κ_{eff} is computed as the effective eddy diffusivity defined in Chen and Plumb (2014):

$$\kappa_{\text{eff}} = -\frac{1}{2\pi \cos\phi_e}\left(\frac{\partial Q}{\partial \phi_e}\right)^{-1}$$
$$\times \left(\iint_{q_g>Q,\phi\leq\phi_e(Q)} \dot{q}_g\, d\mathbf{S} - \iint_{q_g\leq Q,\phi>\phi_e(Q)} \dot{q}_g\, d\mathbf{S} \right), \tag{6}$$

where $\dot{q}_g$ denotes the small-scale diffusion acting on the PV. Physically speaking, κ_{eff} represents the stretching, deformation, filamentation, and cutoff of PV contours, as indicated by Fig. 1, and it encapsulates all these eddy processes that lead to a downscale cascade of variance until it is halted by small-scale diffusion (Nakamura and Zhu 2010), which is primarily barotropic until the variance is ultimately removed by the vertical or diabatic diffusion at small scales (Leibensperger and Plumb 2014). As in Nie et al. (2014), these first two terms on the RHS of Eq. (5) will be here denoted as the baroclinic term and barotropic term, respectively. The third term is negative wave activity tendency, denoted by wave transience, which describes the conservative (i.e., frictionless and adiabatic) propagation of waves that lead up to the growth or decay of wave amplitude. In this study, diabatic sources and sinks of wave activity have been ignored, as they are weak in the upper troposphere.
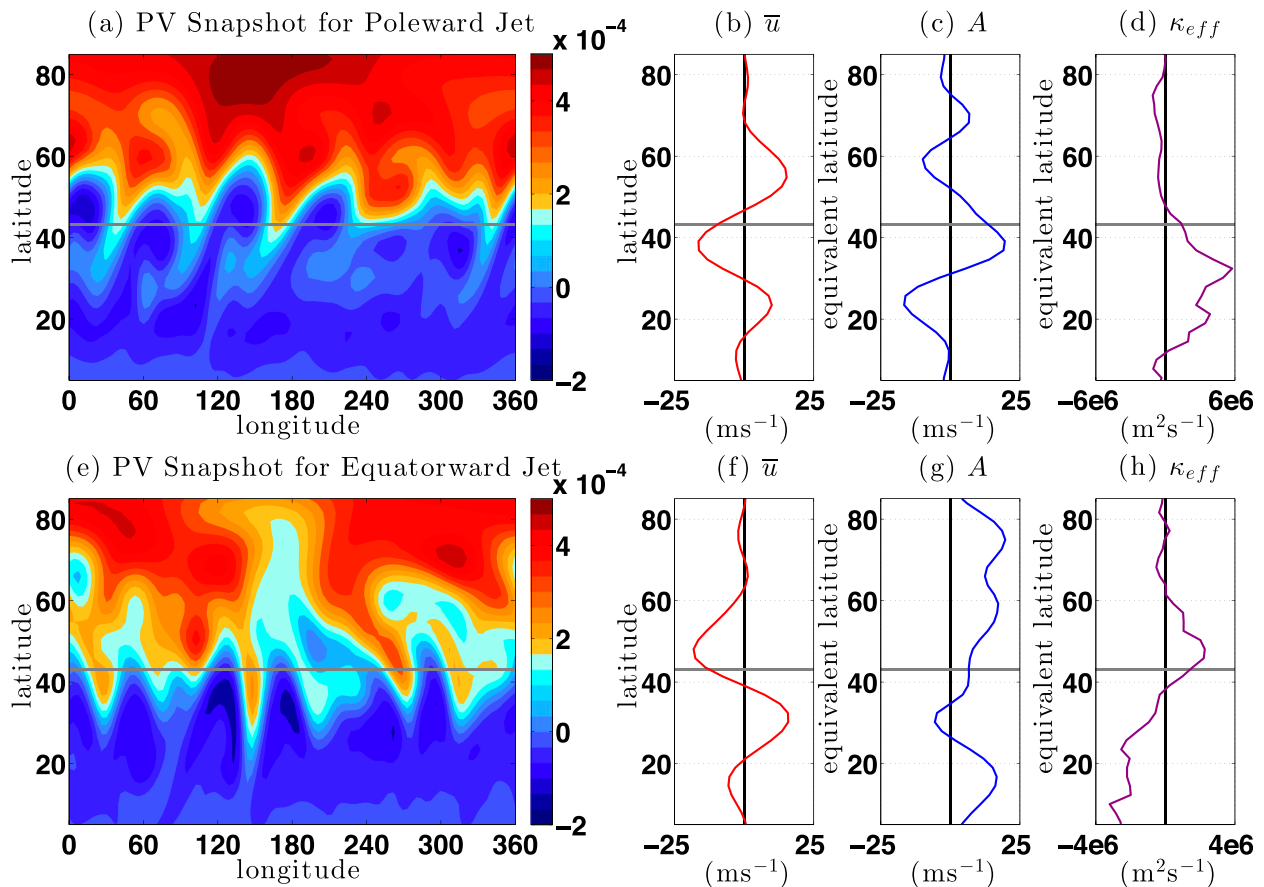
FIG. 4. Control run snapshots of 250-hPa (a),(e) quasigeostrophic potential vorticity (s^{-1}), (b),(f) zonal-mean zonal wind anomaly, (c),(g) wave activity anomaly, and (d),(h) effective diffusivity anomaly (all from climatology) for a day when the zonal index is in a (top) positive and (bottom) negative phase. The horizontal gray line in each plot indicates the climatological jet latitude. Units are shown on the x axis for each line plot.

Together, these form a wave activity budget based on the contour averaging for wave activity and effective diffusion and the standard gridpoint calculations of eddy momentum flux convergence, M, and vertical wave activity flux convergence, underpinning the hybrid Eulerian–Lagrangian diagnostic.

The physical interpretations of these above terms are illustrated schematically in Fig. 1 for both the poleward-shifting (top row) and equatorward shifting (bottom row) jet stream, analogous to the positive and negative phases of the annular mode. For the positive phase, waves predominately grow on the equatorward flank of the climatological jet, leading to stretching and fila-mentation of PV contours. As the waves continue to grow, they enter a region of anticyclonic shear on the equatorward flank of the jet. With enough shear, the waves can grow beyond a small-amplitude limit and break as indicated by the reversal in PV meridional gradient. Cutoff lobes of high-PV air can develop, leading to a slowly dissipating PV anomaly. It is the slow dissipation described by the barotropic term of

irreversible PV mixing along with the continual pump-ing of vertically converging waves from the baroclinic term that lead to the poleward jet shift for this example. The opposite is true for an equatorward shift of the midlatitude jet stream where waves predominantly grow on the poleward flank of the jet in a cyclonically sheared environment, leading to cyclonic wave breaking and slow dissipation of low-PV air on the poleward flank of the climatological jet. This is concurrent with a persis-tently equatorward zonal wind anomaly.

Figure 4 further clarifies key aspects of the wave ac-tivity formalism introduced in Eq. (5) by using the control run. The top- and bottom-row plots are a snap-shot of PV on a particular day when the zonal-mean zonal wind is poleward and equatorward, respectively, of its climatological position (horizontal gray line), similar to the schematic in Fig. 1. Nakamura and Zhu (2010) formally proved that $A + \overline{u}$ is constant for a barotropic conservative flow, so there is an exchange between anomalously high zonal wind and anomalously low wave activity, and vice versa. Generating these

anomalous wave activity signatures are the large undulations from zonal symmetry in the PV fields in Figs. 4a and 4e, where high-PV air is advecting south and low-PV air is advecting north. When waves are predominately concentrated on the equatorward flank of the jet, in Figs. 4a–d, there is an anticyclonic shear tendency that tilts the waves to the northeast, indicating poleward momentum fluxes. This enhances the jet on its poleward flank (Fig. 4b) where there is anomalously low wave activity (Fig. 4c). The large waves on the equatorward flank of the jet produce an anomalously large κ_{eff} signature (Fig. 4d), where contour stretching, filamentation, or wave breaking is evident. In contrast, for a jet in an equatorward position in Figs. 4e–h, anomalously small wave activity values on the equatorward flank of the jet are associated with anomalously small κ_{eff} values and large zonal wind anomalies concurrent with northwest-tilted troughs and ridges associated with the cyclonic shear on the poleward flank of the climatological jet. Therefore, the two above cases exemplify that the high and low index states of the annular modes are associated with similar but opposite-signed meridional dipoles in the zonal wind, wave activity, and eddy mixing distribution.

To better understand the temporal evolution of eddy momentum forcing associated with the annular mode variability, lagged regressions between z and the upper-level vertical average of Eq. (5) are performed. For any variable, this upper-level vertical average is defined as $\langle X \rangle_{\mathrm{up}} = (1/p_s) \int_{100\mathrm{hPa}}^{500\mathrm{hPa}} X \, dp$, where up represents the upper-level average. Applying this vertical average to Eq. (5) yields

$$\langle M \rangle \approx \langle M \rangle_{\mathrm{up}} = -f \left\langle \frac{\partial}{\partial p} \left(\frac{\overline{v'\theta'}}{\overline{\theta}_p} \right) \right\rangle_{\mathrm{up}} - \left\langle \frac{\kappa_{\mathrm{eff}}}{a} \frac{\partial Q}{\partial \phi_e} \right\rangle_{\mathrm{up}}$$
$$- \frac{\partial \langle A \rangle_{\mathrm{up}}}{\partial t}, \qquad (7)$$

where we have used the fact that eddy momentum flux is concentrated in the upper troposphere between 100 and 500 hPa.

Shown in Fig. 5 are the lagged regressions performed on Eq. (7), which reveal details of the momentum forcing of the zonal wind. This zonal wind shift is highly persistent, extending beyond lag ±50 days. As expected from Eq. (3), the eddy momentum flux convergence shows evidence that the annular mode is not only initially eddy driven but is also eddy sustained. Contributing to this eddy driving are two seemingly different time scales. The tilt in wave transience phase line indicates an equatorward wave propagation that takes place on the time scale of a baroclinic eddy life cycle.

Wave transience contributes to a rapid acceleration/deceleration pattern centered near lag ±7 days, while the baroclinic and barotropic terms sustain a poleward eddy driving beyond ±50 days.

Furthermore, plotted in Fig. 5e is the full barotropic term $[-(\kappa_{\mathrm{eff}}/a)(\partial Q/\partial \phi_e)]$ and in Fig. 5f is the contribution from the κ_{eff}. While the change in the meridional gradient of Lagrangian potential vorticity indicates regions of jet enhancement or suppression, κ_{eff} indicates regions of contour stretching, filamentation, and breaking. Large κ_{eff} values (i.e., contours stretched meridionally from zonal symmetry) coincide with enhanced RWB (Nie et al. 2014), so it will be used in this study to analyze changes in the geometry of PV contours, as illustrated in Figs. 4d and 4h. The reduction in mixing on the poleward flank of the jet indicates a more zonally symmetric PV field: that is, less RWB (see Fig. 4a) and a poleward sustained jet. This can be thought of as the poleward-shifted jet sustaining a mixing barrier leading to less mixing on the poleward flank and more mixing on the equatorward flank of the climatological jet (e.g., Nakamura 1996; Haynes and Shuckburgh 2000; Chen and Plumb 2014). The wave activity analysis elucidates that persistently less mixing on the jet's poleward flank in the upper level along with a persistent baroclinic pumping of wave activity from the lower level act constructively to sustain a persistently poleward jet, as observed in the southern annular mode (e.g., Nie et al. 2014).

It is noteworthy that this indicates an asymmetry between the positive and negative phases of the annular modes as a result of the preferred equatorward wave propagation on the sphere (e.g., Barnes et al. 2010). The equatorward wave propagation, as indicated by the phase line of wave activity transience within lag ±7 days, is followed by anomalous effective diffusivity and westerlies near 20° latitude in lag 10–20 days. The subsequent interaction with the Hadley cell provides additional asymmetry, shown in Simpson et al. (2012), that is absent in a quasigeostrophic (QG) model (e.g., Zhang et al. 2012). It will be shown in the next section that this asymmetry becomes more pronounced as the eddy-driven jet moves poleward in response to idealized thermal forcing.

c. Quantification of feedback

A compact analysis of eddy feedback mechanisms, as in Simpson et al. (2013) and Nie et al. (2014), can be demonstrated by first computing the time series through projecting $\langle \overline{X} \rangle$ onto the leading **E** as $x(t) = \langle \overline{X} \rangle \mathbf{WE}/\mathbf{EWE}$, where x indicates the portion of $\langle \overline{X} \rangle$ that projects onto **E**, and **W** is the diagonal weighting matrix of $\cos\phi$ (Baldwin et al. 2009).
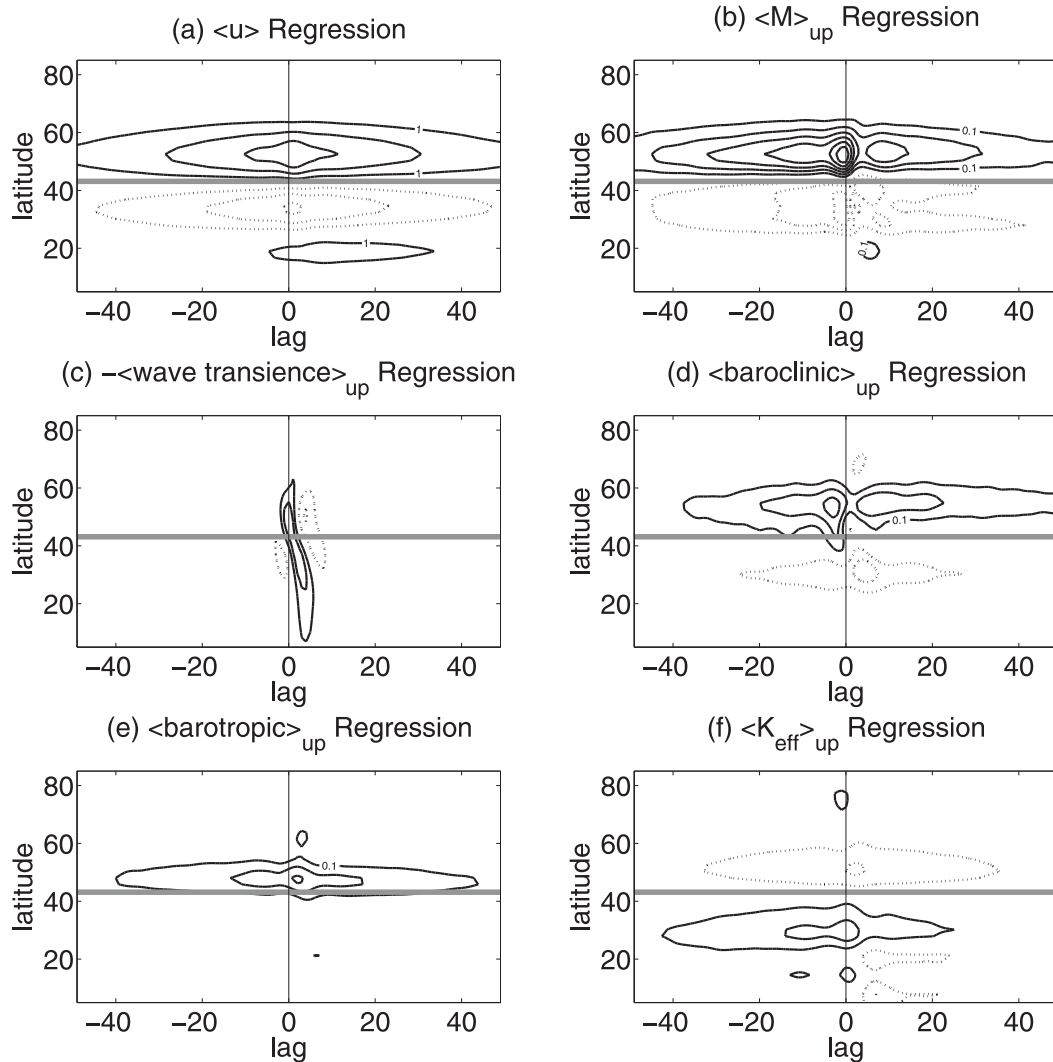
FIG. 5. Control run lagged regressions onto the zonal index for (a) zonal-mean zonal wind (m s^{-1}), (b) eddy momentum flux convergence (m s^{-1} day^{-1}), (c) wave transience (m s^{-1} day^{-1}), (d) eddy-heat flux convergence (baroclinic term, m s^{-1} day^{-1}), (e) irreversible mixing of quasigeostrophic potential vorticity (full barotropic term, m s^{-1} day^{-1}), and (f) effective diffusivity (m^2 s^{-1}), all vertically averaged from 500 to 100 hPa, except $\overline{u}$ that is averaged down to the surface. Negative lags indicate that the eddy time series leads the zonal index, while for positive lags, the zonal index leads. Negative contours are dotted. The contour interval for the effective diffusivity is 6×10^4 m^2 s^{-1}. The horizontal gray line in each plot indicates the climatological jet latitude.

It follows that the zonal-mean zonal wind tendency [Eq. (3)] and wave activity budget [Eq. (7)] can be projected onto the annular mode as (Nie et al. 2014)

$$\frac{\partial z}{\partial t} = m_{up} - \frac{z}{D}$$
$$m_{up} = m_{bc} + m_{bt} + m_A,$$

(8)

where subscripts up, bc, bt, and A denote upper-level eddy momentum flux convergence, baroclinic, barotropic, and wave transience terms, respectively. The time scale of frictional damping acting on the annular mode is denoted by D.

A lagged-covariance structure between the eddy forcing time series in Eq. (8) and z is displayed in Fig. 6a, where a positive value indicates an eddy forcing that supports a poleward jet, and positive lags indicate z leads the eddy forcing time series. As for the observed annular mode (Lorenz and Hartmann 2001), the black dashed–dotted line shows the eddy momentum flux convergence contribution with positive values in both negative and positive lags that separately drive the jet poleward and sustain the jet at a poleward position. The contribution from wave transience indicates, as in Fig. 5c, a positive contribution near lag −5 followed by a
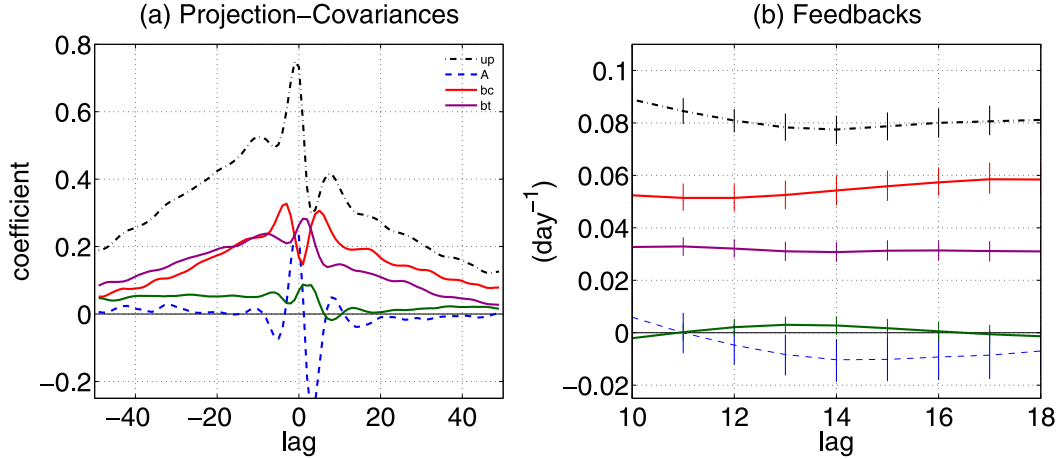
FIG. 6. Control run eddy momentum flux convergence (dashed–dotted black line), wave transience (dashed blue line), baroclinic term (red line), barotropic term (purple line), and residual (green line) of (a) the lagged covariance of eddy time series in Eq. (8) onto the zonal index $[(\text{m s}^{-1})^2 \text{ day}^{-1}]$ and (b) feedback strengths. Vertical lines in (b) indicate the 95% confidence intervals based on 1000 bootstraps.

rapid drop to negative after lag 0. This short-term behavior may be attributed to a transient eddy life cycle response to the zonal wind variability. In contrast, the baroclinic and barotropic contributions, in agreement with Figs. 5d and 5e, can both initiate and maintain the jet in a poleward state, as indicated by the positive value throughout the entire lag period. There is also a small residual in the wave activity budget, which can be attributed to the diabatic source of wave activity, QG approximation, or numerical errors in computing the budget. Nie et al. (2014) computed the barotropic term associated with the annular mode variability indirectly as a residual in the wave activity budget. The direct calculation by means of the small-scale diffusion used in the model [Eq. (6)], as shown here, confirms that the direct and indirect calculations of the barotropic term agree well. For all the simulations examined in this study, this residual term is negligible except for the most poleward simulations.

In comparison with the lagged covariance between the eddy forcing and z in the observed southern annular mode variability [cf. Fig. 2 of Nie et al. (2014)], these results are qualitatively similar yet exhibit some quantitative differences. First, as mentioned above, the time scale is overly persistent as a result of the idealized model physics and coarse model resolution, and thus the overall momentum forcing strengths in lags from about +10 to +30 days are excessively strong and support the highly persistent poleward wind shift that is not evident in the observations. While the covariance of wave transience and barotropic term are of the same order of magnitude as compared with the observations, the baroclinic term is much larger than the observed values. It is also positive throughout these lags, whereas in observations it is

negative at small negative lags [cf. Fig. 2 of Nie et al. (2014)]. This may suggest a baroclinic mechanism as the cause of an overly persistent jet in addition to non-modeled moisture processes (Xia and Chang 2014) and zonal asymmetries, such as mountains (Gerber and Vallis 2007), that have been shown to reduce the annular mode time scale.

Additionally, Lorenz and Hartmann (2001) suggested that the forcing of z can be separated into two components such that m_{up} in Eq. (8) can be parameterized as the random component $\tilde{m}_{up}$ that initiates a zonal wind shift plus the linearly dependent, eddy feedback part $b_{up}z$, where b_{up} represents the feedback strength. Decomposing the eddy momentum forcing time series m_{up} into its components gives

$$m_{up} = \tilde{m}_{up} + b_{up}z = \tilde{m}_{up} + b_{bc}z + b_{bt}z + b_A z, \quad (9)$$

where b_{up}, b_{bc}, b_{bt}, and b_A are the feedback strengths for their respective terms. Simpson et al. (2013) showed that the individual contributions from synoptic-scale and planetary-scale waves to eddy feedback can be estimated through lagged-regression analysis, which was used by Nie et al. (2014) to separate the three feedback mechanisms above. Regressing the time series of m_{up} and z onto z with a lag of Δt implies that $m_{up}(t + \Delta t) \approx \beta_m^{\Delta t} z(t)$ and $z(t + \Delta t) \approx \beta_z^{\Delta t} z(t)$, where $\beta_m^{\Delta t}$ and $\beta_z^{\Delta t}$ are the regression coefficients of m_{up} and z at lag Δt, respectively. At large lags, the random component of the eddy forcing, $\tilde{m}_{up}$, should be nearly zero since the eddy forcing is mainly driven by the zonal flow at these lags. This implies that the feedback strength can be computed as $b_{up}^{\Delta t} = \beta_m^{\Delta t} / \beta_z^{\Delta t}$. Similarly, replacing $\beta_m^{\Delta t}$ with $\beta_{bc}^{\Delta t}$, $\beta_{bt}^{\Delta t}$, and $\beta_A^{\Delta t}$ in this linear
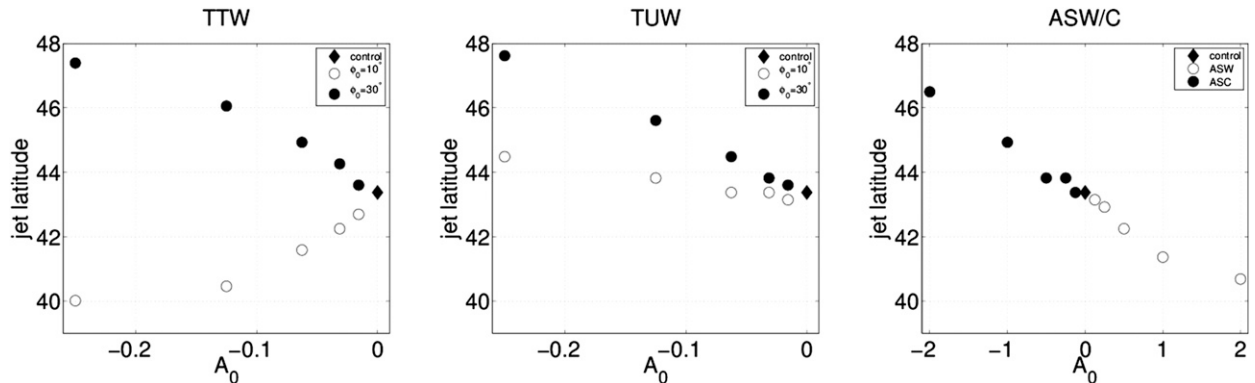
FIG. 7. Climatological jet latitude as a function of forcing strength for (left) TTW, (middle) TUW, and (right) ASW/C runs. Black-filled circles indicate broad warming runs (e.g., $\phi_0 = 30°$; e.g., negative values of A_0); open circles are for $\phi_0 = 10°$ runs; and black diamonds are for the control runs.

model will provide a quantitative structure of the feed-back strengths as a function of large lag.

Figure 6b gives these feedback strengths as a function of lag for each process. The relatively constant feedback strength indicates the validity of this linear model. A positive feedback indicates a supporting role in maintaining a jet shift, while a negative feedback indicates a dampening of z. Also provided in the plot are the 95% confidence intervals associated with the bootstrap method described in Simpson et al. (2013). The method randomly samples the daily data with re-placements to compute confidence intervals of the feedback strength. For each lag day, 1000 bootstraps are performed to provide a large sample of possible feed-back values. The two-tailed confidence intervals are then determined for the 1000 random samples, indicated by vertical lines for each process and lag. The black line indicates the total eddy feedback that is reinforced by the anomalous zonal flow. Contributing to this positive eddy feedback are both the baroclinic and barotropic processes, while the wave transience plays only a small role in the feedback at large lags, consistent with Fig. 5. The lack of a residual demonstrates both the strength of the wave activity formalism in describing eddy–mean flow interaction and the strength of the feedback anal-ysis performed. Overall, there is good agreement be-tween the modeled variability and the observed annular mode variability (Nie et al. 2014). Hence, an average of these feedback strengths can be taken over a range of lag values to obtain a single measure of feedback strength.

4. Response of annular mode time scales to thermal forcings

Having illustrated the wave activity diagnostic with the control run, this section uses idealized thermal

perturbations to move the latitude of the eddy-driven jet and assess the effects on the strength of different feed-back processes.

Figure 7 summarizes the direction of the jet shift with respect to the magnitude of the individual thermal forcings that have been elaborated in section 2. The response is approximately linear to the magnitude of the forcing, yielding a range of jet latitudes. Again, these jets do not reach latitudes as far poleward of the SH eddy-driven jet, but the experiments were designed to provide a range of possible jet latitudes to analyze. The response to the TTW narrow warmings is an equator-ward shift of the zonal jet and to broad warmings a poleward shift. Both narrow and broad warmings for the TUW runs shift the jets poleward. The ASW scenarios shift all the jets equatorward, while the ASC scenarios shift the jets poleward. As the mechanisms of the cli-matological jet responses to tropical warming have been examined in Sun et al. (2013) and Lu et al. (2014), the question now becomes, how does the climatological jet latitude affect the time scale associated with the annular mode?

The autocorrelations of z are plotted in Fig. 8a to highlight the persistence associated with different cli-matological jet latitudes. The colors within the plot de-pict the latitude of the climatological jet, where the blue represents a more poleward jet, and red represents a more equatorward jet. As a jet moves farther equator-ward (redder), the jet becomes more persistent, that is it takes longer to fall below the e-folding threshold, which is consistent with other modeling efforts (Barnes et al. 2010; Garfinkel et al. 2013). The dependence of the an-nular mode time scale on jet latitude can be summarized with a calculation of τ, the e-folding time scale. In Fig. 8b, this shows that, as the climatological jet latitude increases, there is a tendency for a decrease in annular
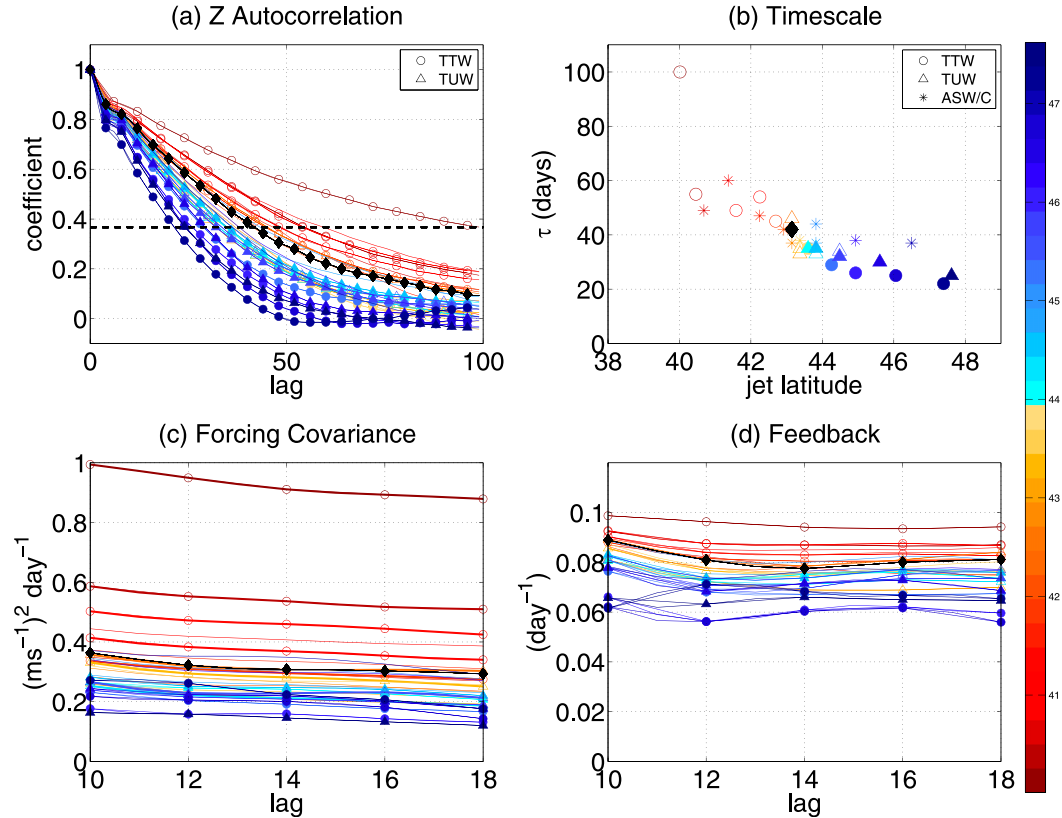
FIG. 8. (a) The zonal index lagged autocorrelation (only positive lags shown) for the TTW (circles) and TUW (triangles) runs. The horizontal black dashed line indicates the e-folding time scale. (b) The e-folding time scale as a function of climatological jet latitude for the TTW and TUW runs as in (a) and for the ASW/C (asterisks) and the control run (diamonds). (c) Lagged covariance of m_{up} in Eq. (8) with zonal index for positive lags when zonal index leads m_{up}. (d) Eddy momentum flux convergence feedback strength b_{up} as a function of positive lag. The colors for all plots indicate the latitude of the jet with warmer (red) colors for equatorward jet latitudes and cooler (blue) colors for poleward jet latitudes. Black lines and shapes represent the control run. Shapes for (a),(c), and (d) are indicated in (a), and shapes for (b) are indicated in (b), with nonfilled shapes representing narrow warming runs and filled shapes representing broad warming runs.

mode time scales, showcasing a fairly linear relationship similar to the Coupled Model Intercomparison Project, phase 3 (CMIP3; Barnes and Hartmann 2010).

This same persistence feature can be noted in Fig. 8c which plots the lagged covariance of m_{up} in Eq. (8) with respect to z for large positive lags where eddy feedbacks are expected. Consistent with the τ calculations, there is a general tendency to reduce the eddy feedback strength on the annular mode with an increase in jet latitude, where a poleward jet is reinforced by a much weaker eddy feedback compared with an equatorward jet. The total feedback strength associated with the eddy momentum flux convergence, $b_{up} = \beta_m^{\Delta t}/\beta_z^{\Delta t}$, in Fig. 8d exhibits this same feature. The more equatorward the jet latitude, the stronger the eddy feedbacks are. For the majority of the experiments these feedback values are nearly constant over this lag period and give confidence that this linear model is sufficient to quantify eddy

feedback strengths. Collectively, these results corroborate the relationship between the jet latitude and eddy feedback found in the CMIP3 models (Barnes and Hartmann 2010) and that the relationship is controlled by the large-scale eddy–mean flow interactions in the atmosphere.

The robustness of the aforementioned results is verified by repeating the control run and four TTW runs (i.e., standard heating and quadruple heating runs for narrow and broad warming in Table 1) at different horizontal resolutions (i.e., R60, T42, and T85). The length of the R60 and T42 simulations is the same 12 000 days as R30. The T85 simulation is integrated only for 6000 days, but the statistics are consistent with R60. Figure 9 summarizes the same diagnostics as Fig. 8, but for varied horizontal resolutions, with each resolution consisting of five simulations. Similar to the simulations at the R30 resolution, the annular mode
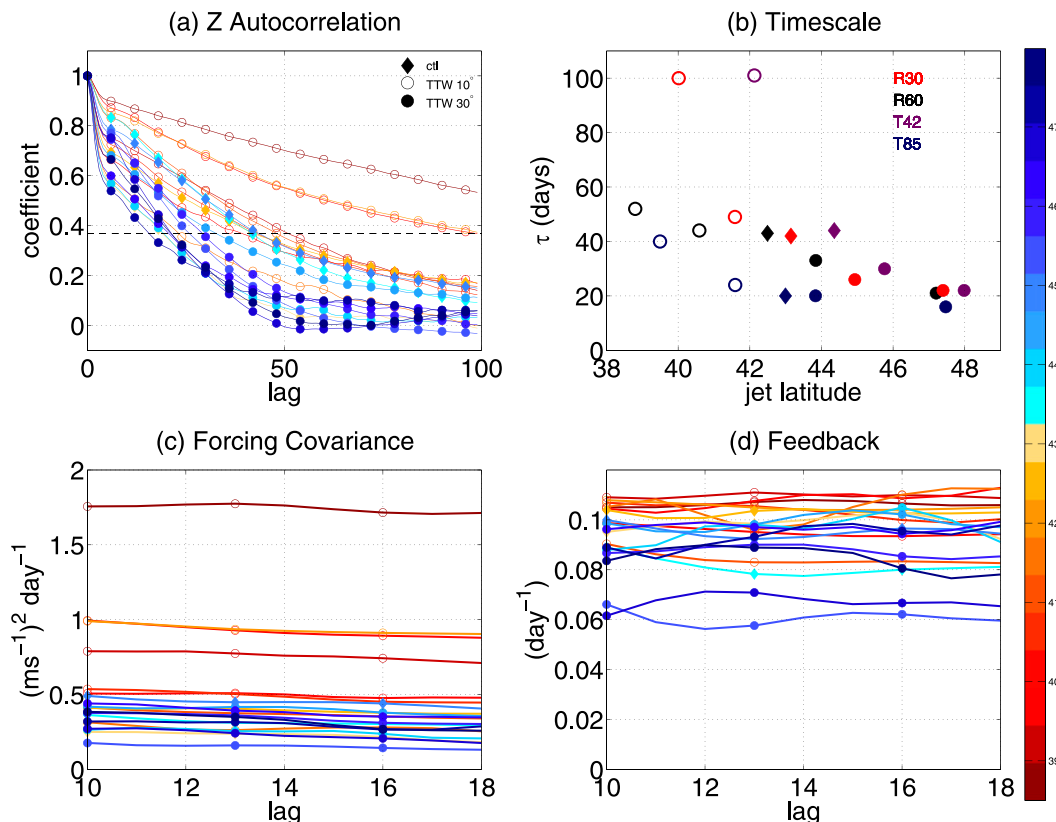
FIG. 9. As in Fig. 8, but the diagnostic is applied to different horizontal resolutions and spectral truncations. In all the plots, open circles indicate the narrow TTW runs, filled circles indicate the broad TTW runs, and diamonds indicate the control runs for each resolution, including R30, R60, T42, and T85. Experiments with the standard heating and quadruple heating are used (see Table 1). In (b), data points are not color coded by jet latitude, as in (a), (c), and (d), but are color coded by their resolution, as indicated by the legend.

variability is more persistent for more equatorward jet latitudes (coded by the redder color), as indicated by the slower decay rate in the autocorrelation function or the larger e-folding time scale. This is also corroborated by enhanced eddy feedback, as evident in the lagged covariance between the eddy momentum forcing and z and the strength of the feedback parameter at different positive lags. Nevertheless, these simulations show a larger spread in the relationship between the annular mode time scale and jet latitude. Particularly, the annular mode time scales for the simulations with the most equatorward jet at R30 and T42 (~100 days) are much larger than those at R60 and T85 (~50 days), and they appear to be outliers in the scatterplot. The overly persistent jet at coarser resolutions is also noted in Gerber et al. (2008b).

The strengths of the individual feedbacks for the R30 simulations, averaged from lag +10 to +18, are plotted as a function of the mean jet latitude in Fig. 10 along with the bootstrapped, two-tailed confidence intervals described above. The total eddy feedback strength in

Fig. 10a shows a strong decay with increasing jet latitude consistent with the zonal index autocorrelation and related τ values. Comparing this with the forcing mechanisms in Eq. (9), it appears the majority of this decrease in eddy feedback is related to the decrease in barotropic eddy mixing as the jet latitude increases. Wave transience plays a negligible role in dampening the annular mode throughout the jet latitudes because of its rapid variability demonstrated in Fig. 5c. In contrast, the baroclinic feedback becomes stronger with an increase in jet latitude, opposite to the trend of the total eddy feedback, indicating that the amplitude of baroclinicity and associated eddy feedback from the baroclinic term are not the most important contribution. The feedback from the residual term also decreases with a more poleward jet latitude. In addition, the R30 simulations described above are qualitatively similar for the simulations with varied horizontal resolutions (not shown here), although the feedback strength exhibits a larger spread across horizontal resolutions, as does the annular mode time scale (Fig. 9). As the hyperdiffusion used in
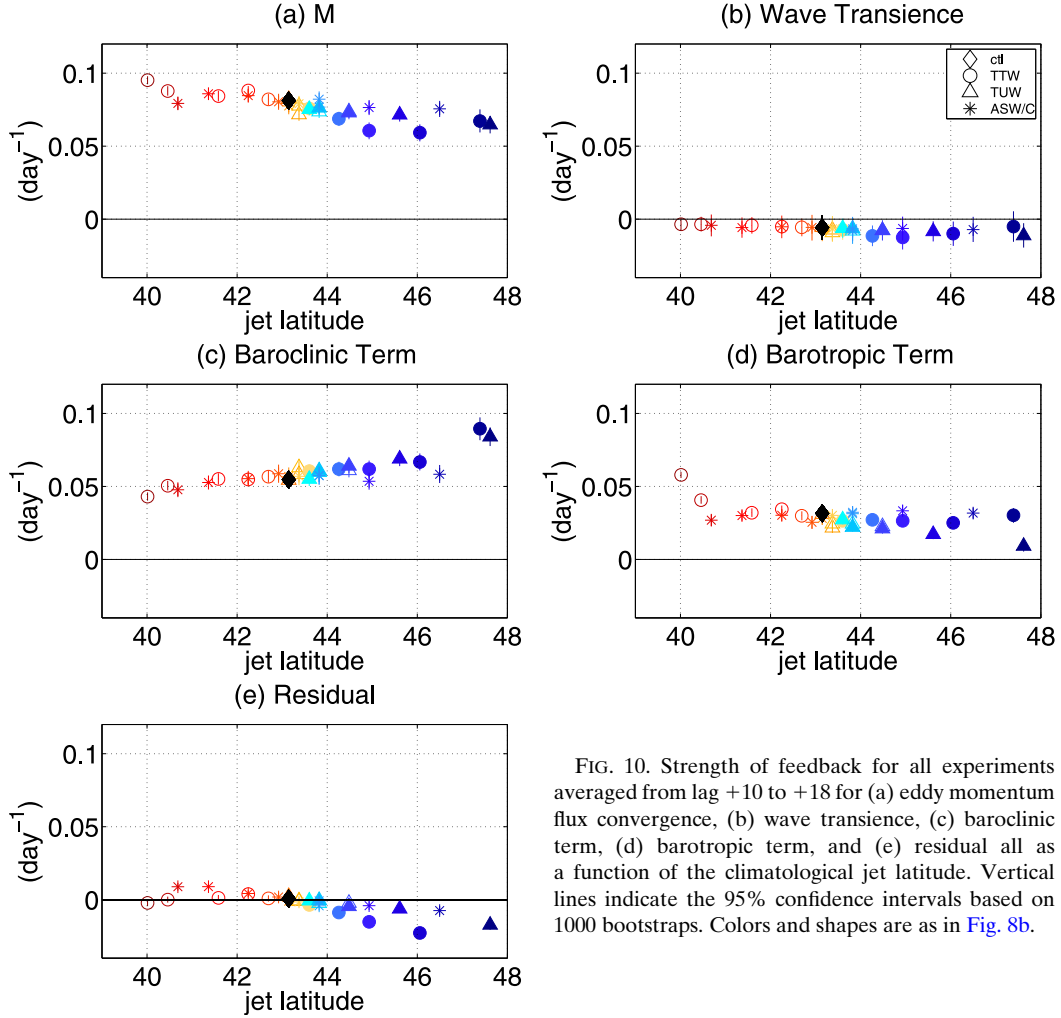
FIG. 10. Strength of feedback for all experiments averaged from lag +10 to +18 for (a) eddy momentum flux convergence, (b) wave transience, (c) baroclinic term, (d) barotropic term, and (e) residual all as a function of the climatological jet latitude. Vertical lines indicate the 95% confidence intervals based on 1000 bootstraps. Colors and shapes are as in Fig. 8b.

the model is scale dependent, the hyperdiffusion is much weaker at higher horizontal resolutions, and thus the fine-scale structure of PV is better resolved. The consistency across horizontal resolutions indicates that the changes in effective diffusivity and associated barotropic feedback with respect to the jet latitude are driven by the large-scale circulation rather than details of the diffusion parameterization.

Furthermore, Chen and Plumb (2009) suggested a quantitative relationship between the eddy feedback b and annular mode time scale τ may be obtained from Eqs. (8) and (9):

$$\tau^{-1} = D^{-1} - b. \qquad (10)$$

For small perturbations, one can obtain $\delta\tau/\tau_0^2 \approx \delta D/D_0^2 + \delta b$, where τ_0 and D_0 are the annular mode time scale and frictional damping time scale in the control run. To the extent that the frictional damping on the annular mode does not change in these model runs [this was confirmed with

calculations of D through techniques described in Chen and Plumb (2009), not shown], one would expect that $\delta\tau$ and δb are positively correlated and that the change in τ may be decomposed by individual eddy feedback mechanisms. Figure 11 plots the feedback strength as a function of τ (the outlier in Fig. 8b with $\tau \sim 100$ days is not plotted). Indeed, there is a nearly linear relationship between $\delta\tau$ and δb, which follows the theoretical time scale (blacked dashed line) considerations very well. Similar conclusions are drawn between this and the previous figure. It is now quite clear that the increase in total feedback strength with τ in Fig. 11 is related to the increase in barotropic feedback strength associated with wave breaking and irreversible PV mixing. Again, wave transience plays a negligibly negative role in dampening the annular mode, the change of baroclinic feedback is opposite to the change of τ, and the residual term is large for the runs with short τ.

What are the mechanisms responsible for the change in annular mode time scale and eddy mixing associated

(a) M

(b) Wave Transience

(c) Baroclinic Term
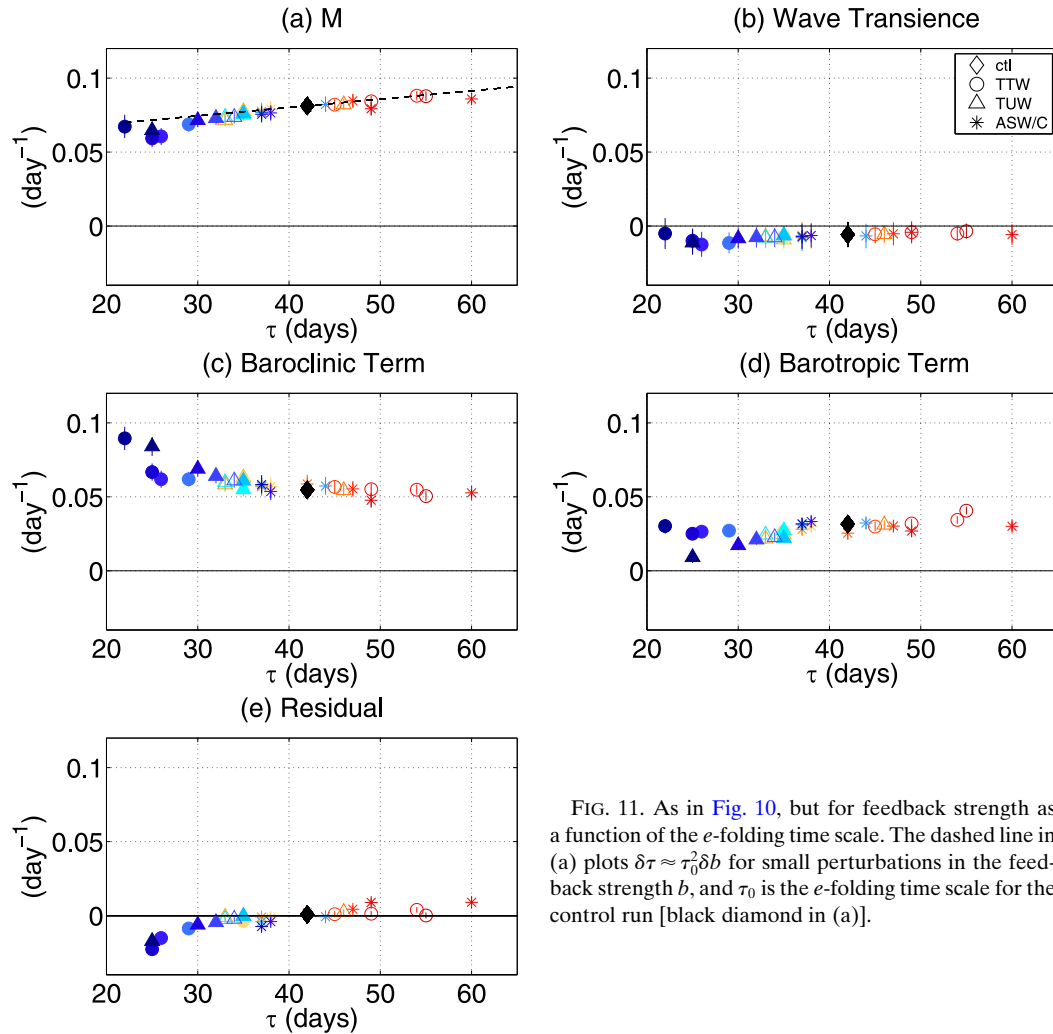
(d) Barotropic Term

(e) Residual

FIG. 11. As in Fig. 10, but for feedback strength as a function of the e-folding time scale. The dashed line in (a) plots $\delta\tau \approx \tau_0^2 \delta b$ for small perturbations in the feedback strength b, and τ_0 is the e-folding time scale for the control run [black diamond in (a)].

with the change in climatological jet latitude? Previous studies have indicated the importance of zonal vacillation and meridionally propagating modes of variability compared to jet latitude (Son and Lee 2006). It is shown that, as the jet latitude increases, the mode transitions from zonal vacillation to meridional propagation. To test this, Fig. 12 plots the zonal-mean zonal wind lag regressions with respect to the zonal index in the first column, the baroclinic term in the second column, and the κ_{eff} in the last column. Results will be shown for the TTW runs, which are consistent with the other experiments in this study. The first row is the most equatorward jet latitude (TTW narrow, quadruple run) and the third row is the most poleward jet latitude (TTW broad, quadruple run); the second row is an intermediate jet latitude (the control run). First, from top to bottom with increasing jet latitude, it is quite clear that the time scale of variability reduces with increasing jet latitude and that the baroclinic pumping and irreversible mixing are

consistent with this. Second, there is an increase in the dipole structure of the baroclinic term with increasing jet latitude. As noted in Fig. 10 and Fig. 11, the baroclinic feedback strength increases for a more poleward jet latitude. This can be interpreted as a strengthening of the baroclinic dipole structure, in Fig. 12h, which will project better onto the $\mathbf{E}$, increasing the baroclinic feedback strength. The reason for the increased dipole strength will be discussed in the next figure. Third, the region of enhanced κ_{eff} on the equatorward flank of the eddy-driven jet, as expected from increased anticyclonic wave breaking during the positive phase of the annular mode, experiences a drastic reduction and even becomes negative for the most poleward jet. Last, there may be a slight hint of an increase in a meridionally propagating mode with increasing jet latitude, but this is not as obvious as in the study of Son and Lee (2006), who used one-point correlation plots. But in all, the reduction in barotropic feedback with increasing jet
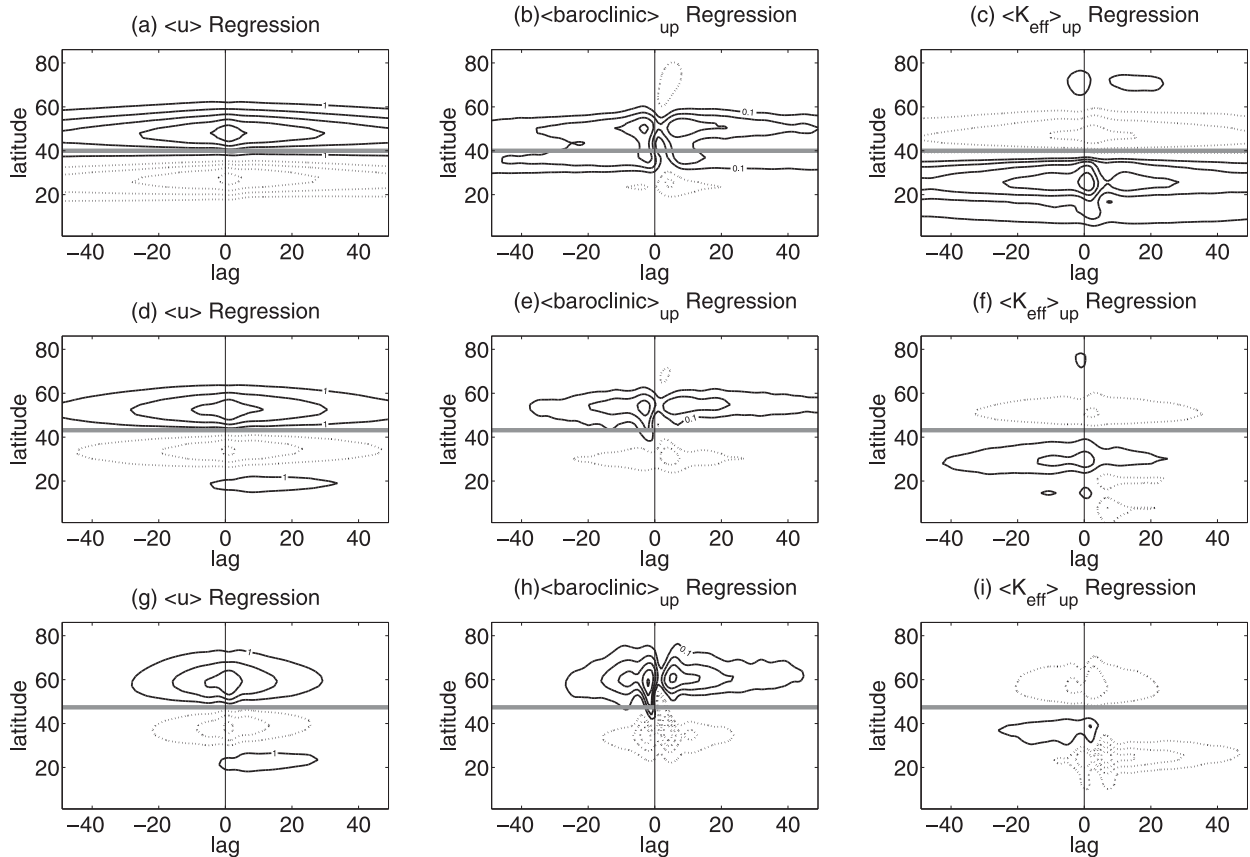
FIG. 12. Lag regressions onto the zonal index for (left) $\langle \overline{u} \rangle$, (center) the $\langle \text{baroclinic} \rangle_{up}$ term, and (right) $\langle \kappa_{\text{eff}} \rangle_{up}$. The contour intervals are, respectively, $1\,\text{m}\,\text{s}^{-1}$, $0.1\,\text{m}\,\text{s}^{-1}\,\text{day}^{-1}$, and $6 \times 10^4\,\text{m}^2\,\text{s}^{-1}$. Dotted contours are negative. (a)–(c) The farthest equatorward jet latitude (TTW narrow, quadruple run), (g)–(i) the farther poleward jet latitude (TTW broad, quadruple run), and (d)–(f) an intermediate jet latitude (the control run). The horizontal gray lines in each plot indicate the climatological jet latitude for the respective run.

latitude that explains the reduction in the annular mode time scale, can be described as a reduction in anomalous κ_{eff} on the equatorward flank of the climatological jet associated with an anomalous poleward jet shift.

Similarly, Fig. 13 shows vertical cross sections of the regressions onto the zonal index (shading) and climatologies (contours) for the zonal wind at lag 0 in the first column, for the baroclinic term and EP vectors at lag +10 days in the second column, and κ_{eff} at lag +10 days in the third column. The climatological structures for each term (note the baroclinic term is not shown for figure clarity) do not change much with increasing jet latitude. The zonal wind regressions demonstrate the shift in annular mode structure in tandem with the climatological jet. The regressions at lag +10 are shown in the second and third column, indicating the eddy feedback induced by the annular mode variability. The overall strength of the baroclinic pumping does not change much with jet latitude, but the wave flux vectors do indicate a slight shift to the poleward flank of the climatological jet. This structure induces less

convergence on the equatorward flank of the jet, which, when vertically averaged to compute projections for feedback calculations, strengthens the dipole structure as mentioned above. This explains the increase in baroclinic feedback strength for more poleward jet latitudes.

Whereas the projection of baroclinic feedback is opposite to the change in total eddy feedback, the irreversible mixing demonstrates a drastic change in the subtropics. On the jet's poleward flank with positive zonal wind anomalies at lag 0, there is a clear reduction in κ_{eff} at lag +10 days in all our simulations, indicating regions where the PV contours exhibit less wave breaking. In contrast, a positive κ_{eff} anomaly in Fig. 13c on the jet's equatorward flank indicates large meridional displacement of PV contours where stretching, filamentation, and breaking are occurring. This positive anomaly fades as the jet latitude increases, until a large region of negative anomalies occurs in the subtropics (Fig. 13i). These are regions where an anomalous subtropical jet has developed (Fig. 13g) and mixing is inhibited or reduced as shown in Simpson et al. (2012). Studies on transport and mixing in the atmosphere have shown
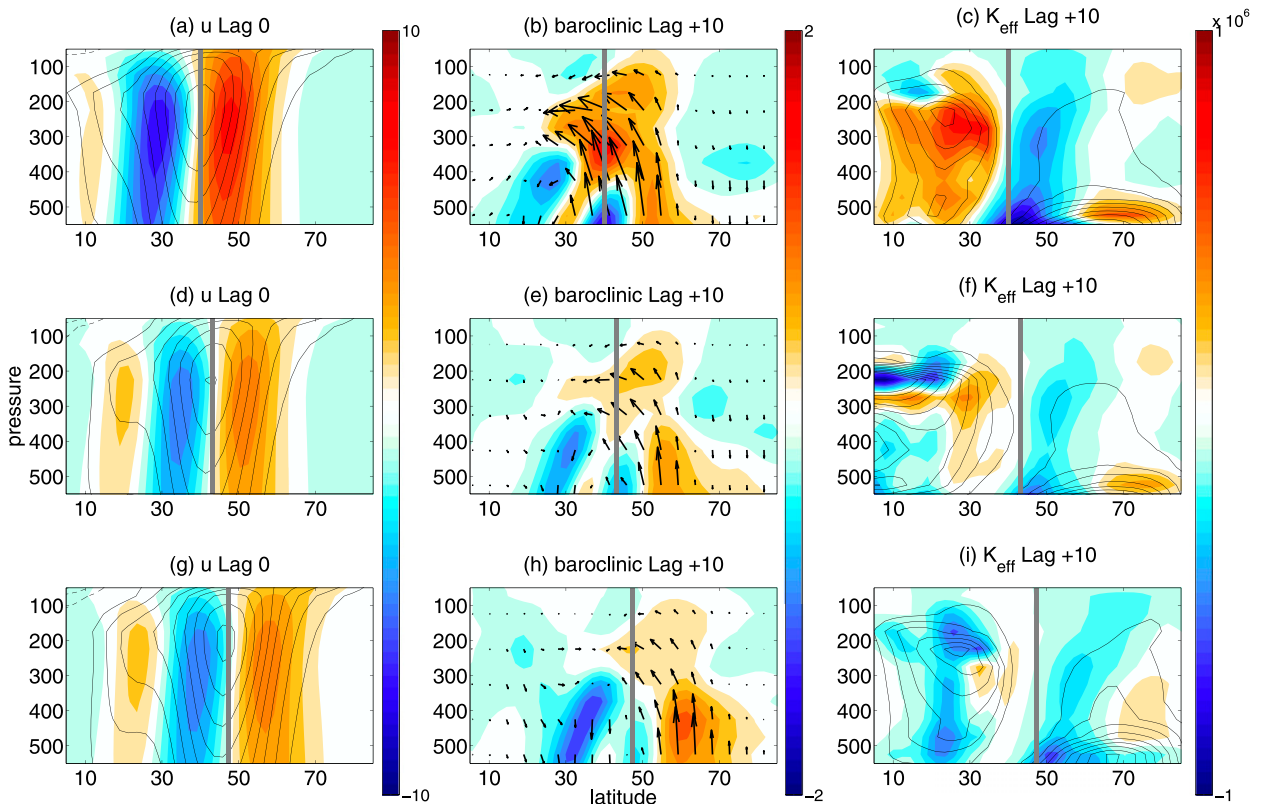
FIG. 13. As in Fig. 12, but vertical cross sections for (left) lag 0 regressions onto the zonal index for $\overline{u}$ (color shading), (center) lag +10 regressions onto the zonal index for the baroclinic term (color shading), and (right) lag +10 regressions onto κ_{eff} (color shading). EP vector regressions are also included in (center) at lag +10 days. Climatologies of $\overline{u}$ and κ_{eff} are in contours. Contour intervals for $\overline{u}$ climatology is $5\,\mathrm{m\,s^{-1}}$ and for the regression is $1\,\mathrm{m\,s^{-1}}$, for the baroclinic term regression is $0.2\,\mathrm{m\,s^{-1}\,day^{-1}}$, and for κ_{eff} climatology is $1 \times 10^6\,\mathrm{m^2\,s^{-1}}$ and for the regression is $1 \times 10^5\,\mathrm{m^2\,s^{-1}}$. Dashed contours are negative.

that a barotropic zonal flow can act as a transport barrier that suppresses eddy mixing (Nakamura 1996; Haynes and Shuckburgh 2000; Chen and Plumb 2014). In particular, this reduction in subtropical eddy mixing may be the anomalous cyclonic shear that has developed when the eddy-driven jet is separate from the subtropical jet, which inhibits the anticyclonic breaking that is typical on the equatorward flank of the jet. Without the positive feedback from subtropical wave breaking, the jet is able to restore toward climatology faster, thus reducing the annular mode time scales. In contrast to Barnes and Hartmann (2010), who emphasize the change in wave breaking on the jet's poleward flank as an explanation for the impact of jet latitude on the annular mode time scale, there is no clear indication of a reduction in anomalous eddy mixing on the poleward flank of the jet in our simulations as the jet latitude increases.

5. Discussion

In this section, the wave activity diagnostic is briefly discussed in comparison with previous studies on the

annular mode variability from the perspective of linear Rossby wave propagation in a zonal flow: wave absorption occurs at the critical latitude, where the eddy phase speed equals the zonal wind, and/or where there is reflection at the turning latitude (e.g., Barnes and Hartmann 2010; Simpson et al. 2012; Lorenz 2014). It is noteworthy that the small-amplitude perturbation of a linear model is often invalid when wave breaking occurs, and thus a parameterization of the eddy–eddy interaction in the surf zone is necessary to produce a realistic distribution for the full spectrum of eddy momentum fluxes. This is achieved by introducing a very large frictional damping in Lorenz (2015), which helps to mimic the surf zone in a linear framework. Regardless of whether the surf zone is parameterized in a linear model or directly simulated in a nonlinear model, one can construct a wave activity budget analogous to Eq. (5), which can quantify individual contributions to the eddy momentum fluxes. The advantage of the wave activity budget used in this study allows us to diagnose individual eddy feedback mechanisms in the observations or idealized or comprehensive models without making any assumption on the small amplitude of eddies.

Using this wave activity diagnostic, the lagged regression of wave activity transience (Fig. 5) portrays a rapid equatorward wave propagation that is followed by subtropical anomalies in effective diffusivity and zonal wind. As the jet moves poleward in response to idealized thermal forcings, the most pronounced change is a reduction in the anomalous subtropical effective diffusivity associated with a separation between the subtropical and eddy-driven jets (Figs. 12, 13). This is in agreement with Simpson et al. (2012), who showed that when the eddy-driven jet system is forced poleward, the range of critical latitudes on the equatorward flank of the jet for waves with different phase speeds increases, resulting in less coherence of wave breaking and subsequently a reduction in the feedback. Within the wave activity framework, the temporal evolution of eddy mixing is negatively correlated with that of zonal wind, which is explained by the effect of zonal wind on transport and mixing (Nakamura 1996; Haynes and Shuckburgh 2000; Chen and Plumb 2014).

The relationship between the zonal wind and eddy mixing may be qualitatively understood by linear theory, which may imply that successes from linear theory in understanding the effect of the beta effect and zonal scale on Rossby wave propagation may be applied to predicting nonlinear wave breaking. For a small perturbation of zonal wavenumber k and phase speed c to a sheared zonal flow $\overline{u}(y)$, the meridional displacement of an air parcel can be understood as $y' \approx \psi'/[\overline{u}(y) - c]$, where the eddy streamfunction $\psi' = \psi_0 \exp[ik(x - ct)]$ and ψ_0 is a constant, and thus it is expected that eddy mixing ($\sim |v'||y'|$) is enhanced where $[\overline{u}(y) - c]$ is smaller (e.g., Green 1970). For a given propagating wave $[c < \overline{u}(y)]$, the zonal wind and eddy mixing are expected to be negatively correlated. Alternatively, linear theory gives the dispersion relationship, $l^2 = (d\overline{q}/dy)/[\overline{u}(y) - c] - k^2$, where l is the meridional wavenumber, and $d\overline{q}/dy$ is the meridional PV gradient. This indicates that a weaker zonal wind would lead to a larger meridional wavenumber or smaller meridional scale, which would, in turn, enhance the effective diffusion, as the small-scale diffusion is scale selective. This perspective emphasizes the consequence of the meridional scale of Rossby waves on effective diffusion, analogous to the ray-tracing theory of wave refraction or reflection (e.g., Barnes and Hartmann 2010; Simpson et al. 2012; Lorenz 2014). This may help to explain the use of very large frictional damping in the linear model of Lorenz (2015) to compensate the lack of wave breaking that otherwise will develop in a nonlinear model. Nevertheless, future investigation is needed to bridge the gap between linear and nonlinear theories in terms of the wave activity budget.

6. Conclusions

Comprehensive climate models with equatorward biases in SH jet latitude are shown to exhibit time scales of variability in the annular mode beyond what is observed (Gerber et al. 2008b; Kidston and Gerber 2010; Barnes and Hartmann 2010) and display greater sensitivity in climate projections, such as increased CO_2 (Woollings et al. 2010; Arakelian and Codron 2012). This study employs the GFDL dry atmospheric dynamical core to examine the effect of climatological jet latitude on eddy feedback strength and the annular mode time scale. Idealized thermal perturbations are used to mimic climate responses, such as tropical temperature warming analogous to ENSO, tropical upper warming analogous to greenhouse gas warming, and Arctic surface warming/cooling analogous to Arctic amplification (e.g., Butler et al. 2010; Sun et al. 2013; Lu et al. 2014). These diabatic perturbations can shift the climatological jet latitude, corroborating the previous studies that a more poleward jet latitude is associated with a reduction in the persistence of the annular mode structure in the eddy-driven jet regime.

Through the use of the finite-amplitude wave activity formalism, the individual contributions to the annular mode time scale from (baroclinic) vertical wave propagation, (barotropic) irreversible PV mixing, and transient growth and decay of waves can be quantified (Chen et al. 2013; Nie et al. 2014). While the barotropic and baroclinic processes are often coupled in a baroclinically unstable system, this separation follows naturally from the wave activity budget. Furthermore, a feedback analysis (Simpson et al. 2013) allows the quantification of feedback strengths for each of the terms in the wave activity formalism (Nie et al. 2014). As the jet latitude shifts poleward, there is a reduction in the total feedback strength that is dominated by a reduction in the barotropic feedback strength, whereas the baroclinic feedback strength is enhanced with increasing jet latitude, and the wave transience is negligible.

Although it has been shown that the subtropical and eddy-driven jets can interact with unforced variability (Eichelberger and Hartmann 2007; Barnes and Hartmann 2011), it was found that a reduction in wave breaking and mixing occurs on the poleward flank of the jet as the climatological jet moves poleward (Barnes et al. 2010). Within the wave activity formalism, the reduction in barotropic feedback as the jet latitude increases is characterized by a weakening in anomalous effective diffusivity on the equatorward flank of the

climatological jet. Since the baroclinic pumping increases with more poleward jet latitudes, the development of a subtropical jet, when the eddy-driven jet is separated, may explain the reduction of effective diffusivity (i.e., reduction in irreversible PV mixing). As waves propagate across the climatological jet into typical regions of anticyclonic shear, the presence of a subtropical jet provides an anomalous cyclonically sheared environment or less anticyclonically sheared environment. This change in shear patterns inhibits the ability for upper-level waves to elongate, tilt to the northeast, and break on the equatorward flank of the climatological jet, as in Fig. 4a. This process may be qualitatively understood as the influence of zonal wind on the size of the meridional displacement of Rossby waves or their meridional scale and the associated eddy mixing (see section 5), analogous to the ray-tracing theory of wave refraction or reflection (e.g., Barnes and Hartmann 2010; Simpson et al. 2012; Lorenz 2014). This reduction in irreversible mixing allows the annular mode structure to shift back to climatology quicker than if slow dissipation of waves were otherwise occurring, as is the case for an equatorward jet.

This above barotropic mechanism is consistent with the transitions in zonal jet variability from zonal vacillation to meridional propagation when the subtropical jet is separated from the eddy-driven jet (Son and Lee 2006). In contrast to Barnes and Hartmann (2010), who emphasize the change in wave breaking on the jet's poleward flank as an explanation for the impact of jet latitude on the annular mode time scale, we found no clear indication of a reduction in eddy mixing on the poleward flank of the jet as the jet latitude increases. Future work is warranted to extend the diagnoses from this idealized dry model to CMIP models.

REFERENCES

Arakelian, A., and F. Codron, 2012: Southern Hemisphere jet variability in the IPSL GCM at varying resolutions. *J. Atmos. Sci.*, **69**, 3788–3799, doi:10.1175/JAS-D-12-0119.1.

Baldwin, M. P., and T. J. Dunkerton, 2001: Stratospheric harbingers of anomalous weather regimes. *Science*, **294**, 581–584, doi:10.1126/science.1063315.

——, D. B. Stephenson, D. W. J. Thompson, T. J. Dunkerton, A. J. Charlton, and A. O'Neill, 2003: Stratospheric memory and skill of extended-range weather forecasts. *Science*, **301**, 636–640, doi:10.1126/science.1087143.

——, ——, and I. T. Jolliffe, 2009: Spatial weighting and iterative projection methods for EOFs. *J. Climate*, **22**, 234–243, doi:10.1175/2008JCLI2147.1.

Barnes, E. A., and D. L. Hartmann, 2010: Testing a theory for the effect of latitude on the persistence of eddy-driven jets using CMIP3 simulations. *Geophys. Res. Lett.*, **37**, L15801, doi:10.1029/2010GL044144.

——, and ——, 2011: Rossby wave scales, propagation, and the variability of eddy-driven jets. *J. Atmos. Sci.*, **68**, 2893–2908, doi:10.1175/JAS-D-11-039.1.

——, ——, D. M. W. Frierson, and J. Kidston, 2010: Effect of latitude on the persistence of eddy-driven jets. *Geophys. Res. Lett.*, **37**, L11804, doi:10.1029/2010GL043199.

Benedict, J. J., S. Lee, and S. B. Feldstein, 2004: Synoptic view of the North Atlantic Oscillation. *J. Atmos. Sci.*, **61**, 121–144, doi:10.1175/1520-0469(2004)061<0121:SVOTNA>2.0.CO;2.

Butchart, N., and E. E. Remsberg, 1986: The area of the stratospheric polar vortex as a diagnostic for tracer transport on an isentropic surface. *J. Atmos. Sci.*, **43**, 1319–1339, doi:10.1175/1520-0469(1986)043<1319:TAOTSP>2.0.CO;2.

Butler, A. H., D. W. J. Thompson, and R. Heikes, 2010: The steady-state atmospheric circulation response to climate change–like thermal forcings in a simple general circulation model. *J. Climate*, **23**, 3474–3496, doi:10.1175/2010JCLI3228.1.

Chen, G., and P. Zurita-Gotor, 2008: The tropospheric jet response to prescribed zonal forcing in an idealized atmospheric model. *J. Atmos. Sci.*, **65**, 2254–2271, doi:10.1175/2007JAS2589.1.

——, and A. R. Plumb, 2009: Quantifying the eddy feedback and the persistence of the zonal index in an idealized atmospheric model. *J. Atmos. Sci.*, **66**, 3707–3720, doi:10.1175/2009JAS3165.1.

——, and ——, 2014: Effective isentropic diffusivity of tropospheric transport. *J. Atmos. Sci.*, **71**, 3499–3520, doi:10.1175/JAS-D-13-0333.1.

——, J. Lu, and L. Sun, 2013: Delineating the eddy–zonal flow interaction in the atmospheric circulation response to climate forcing: Uniform SST warming in an idealized aquaplanet model. *J. Atmos. Sci.*, **70**, 2214–2233, doi:10.1175/JAS-D-12-0248.1.

Edmon, H. J. J., B. J. Hoskins, and M. E. McIntyre, 1980: Eliassen–Palm cross sections for the troposphere. *J. Atmos. Sci.*, **37**, 2600–2616, doi:10.1175/1520-0469(1980)037<2600:EPCSFT>2.0.CO;2.

Eichelberger, S. J., and D. L. Hartmann, 2007: Zonal jet structure and the leading mode of variability. *J. Climate*, **20**, 5149–5163, doi:10.1175/JCLI4279.1.

Feldstein, S. B., and S. Lee, 1998: Is the atmospheric zonal index driven by an eddy feedback? *J. Atmos. Sci.*, **55**, 3077–3086, doi:10.1175/1520-0469(1998)055<3077:ITAZID>2.0.CO;2.

Franzke, C. L. E., S. Lee, and S. B. Feldstein, 2004: Is the North Atlantic Oscillation a breaking wave? *J. Atmos. Sci.*, **61**, 145–160, doi:10.1175/1520-0469(2004)061<0145:ITNAOA>2.0.CO;2.

Fyfe, J. C., and O. A. Saenko, 2006: Simulated changes in the extratropical Southern Hemisphere winds and currents. *Geophys. Res. Lett.*, **33**, L06701, doi:10.1029/2005GL025332.

Garfinkel, C. I., D. W. Waugh, and E. P. Gerber, 2013: The effect of tropospheric jet latitude on coupling between the stratospheric polar vortex and the troposphere. *J. Climate*, **26**, 2077–2095, doi:10.1175/JCLI-D-12-00301.1.

Gerber, E. P., and G. K. Vallis, 2005: A stochastic model for the spatial structure of annular patterns of variability and the North Atlantic Oscillation. *J. Climate*, **18**, 2102–2119, doi:10.1175/JCLI3337.1.

——, and ——, 2007: Eddy–zonal flow interactions and the persistence of the zonal index. *J. Atmos. Sci.*, **64**, 3296–3311, doi:10.1175/JAS4006.1.

——, L. M. Polvani, and D. Ancukiewicz, 2008a: Annular mode time scales in the Intergovernmental Panel on Climate Change Fourth Assessment Report models. *Geophys. Res. Lett.*, **35**, L22707, doi:10.1029/2008GL035712.

——, S. Voronin, and L. M. Polvani, 2008b: Testing the annular mode autocorrelation time scale in simple atmospheric general circulation models. *Mon. Wea. Rev.*, **136**, 1523–1536, doi:10.1175/2007MWR2211.1.

Gillett, N. P., and D. W. J. Thompson, 2003: Simulation of recent Southern Hemisphere climate change. *Science*, **302**, 273–275, doi:10.1126/science.1087440.

Green, J. S. A., 1970: Transfer properties of the large-scale eddies and the general circulation of the atmosphere. *Quart. J. Roy. Meteor. Soc.*, **96**, 157–185, doi:10.1002/qj.49709640802.

Hartmann, D. L., 2007: The atmospheric general circulation and its variability. *J. Meteor. Soc. Japan*, **85B**, 123–143, doi:10.2151/jmsj.85B.123.

——, and P. Zuercher, 1998: Response of baroclinic life cycles to barotropic shear. *J. Atmos. Sci.*, **55**, 297–313, doi:10.1175/1520-0469(1998)055<0297:ROBLCT>2.0.CO;2.

Haynes, P. H., and E. Shuckburgh, 2000: Effective diffusivity as a diagnostic of atmospheric transport: 2. Troposphere and lower stratosphere. *J. Geophys. Res.*, **105**, 22 795–22 810, doi:10.1029/2000JD900092.

Held, I. M., and M. Suarez, 1994: A proposal for the intercomparison of the dynamical cores of atmospheric general circulation models. *Bull. Amer. Meteor. Soc.*, **75**, 1825–1830, doi:10.1175/1520-0477(1994)075<1825:APFTIO>2.0.CO;2.

Hoskins, B. J., and T. J. Woollings, 2015: Persistent extratropical regimes and climate extremes. *Curr. Climate Change Rep.*, **1**, 115–124, doi:10.1007/s40641-015-0020-8.

Kidston, J., and E. P. Gerber, 2010: Intermodel variability of the poleward shift of the austral jet stream in the CMIP3 integrations linked to biases in 20th century climatology. *Geophys. Res. Lett.*, **37**, L09708, doi:10.1029/2010GL042873.

Lee, S., and S. B. Feldstein, 1996: Mechanism of zonal index evolution in a two-layer model. *J. Atmos. Sci.*, **53**, 2232–2246, doi:10.1175/1520-0469(1996)053<2232:MOZIEI>2.0.CO;2.

Leibensperger, E. M., and A. R. Plumb, 2014: Effective diffusivity in baroclinic flow. *J. Atmos. Sci.*, **71**, 972–984, doi:10.1175/JAS-D-13-0217.1.

Leith, C. E., 1975: Climate response and fluctuation dissipation. *J. Atmos. Sci.*, **32**, 2022–2026, doi:10.1175/1520-0469(1975)032<2022:CRAFD>2.0.CO;2.

L'Heureux, M. L., and D. W. J. Thompson, 2006: Observed relationships between the El Nino–Southern Oscillation and the extratropical zonal-mean circulation. *J. Climate*, **19**, 276–288, doi:10.1175/JCLI3617.1.

Lorenz, D. J., 2014: Understanding midlatitude jet variability and change using Rossby wave chromatography: Wave–mean flow interaction. *J. Atmos. Sci.*, **71**, 2370–2389, doi:10.1175/JAS-D-13-0201.1.

——, 2015: Understanding midlatitude jet variability and change using Rossby wave chromatography: Methodology. *J. Atmos. Sci.*, **72**, 369–388, doi:10.1175/JAS-D-13-0199.1.

——, and D. L. Hartmann, 2001: Eddy–zonal flow feedback in the Southern Hemisphere. *J. Atmos. Sci.*, **58**, 3312–3327, doi:10.1175/1520-0469(2001)058<3312:EZFFIT>2.0.CO;2.

Lu, J., L. Sun, Y. Wu, and G. Chen, 2014: The role of subtropical irreversible PV mixing in the zonal mean circulation response to global warming–like thermal forcing. *J. Climate*, **27**, 2297–2316, doi:10.1175/JCLI-D-13-00372.1.

Nakamura, N., 1996: Two-dimensional mixing, edge formation, and permeability diagnosed in an area coordinate. *J. Atmos. Sci.*, **53**, 1524–1537, doi:10.1175/1520-0469(1996)053<1524:TDMEFA>2.0.CO;2.

——, and D. Zhu, 2010: Finite-amplitude wave activity and diffusive flux of potential vorticity in eddy–mean flow interaction. *J. Atmos. Sci.*, **67**, 2701–2716, doi:10.1175/2010JAS3432.1.

Nie, Y., Y. Zhang, G. Chen, X.-Q. Yang, and D. A. Burrows, 2014: Quantifying barotropic and baroclinic eddy feedbacks in the persistence of the southern annular mode. *Geophys. Res. Lett.*, **41**, 8636–8644, doi:10.1002/2014GL062210.

Perlwitz, J., S. Pawson, R. L. Fogt, J. E. Nielsen, and W. D. Neff, 2008: Impact of stratospheric ozone hole recovery on Antarctic climate. *Geophys. Res. Lett.*, **35**, L08714, doi:10.1029/2008GL033317.

Ring, M. J., and A. R. Plumb, 2008: The response of a simplified GCM to axisymmetric forcings: Applicability of the fluctuation–dissipation theorem. *J. Atmos. Sci.*, **65**, 3880–3898, doi:10.1175/2008JAS2773.1.

Robinson, W. A., 2000: A baroclinic mechanism for the eddy feedback on the zonal index. *J. Atmos. Sci.*, **57**, 415–422, doi:10.1175/1520-0469(2000)057<0415:ABMFTE>2.0.CO;2.

——, 2006: On the self-maintenance of midlatitude jets. *J. Atmos. Sci.*, **63**, 2109–2123, doi:10.1175/JAS3732.1.

Simmons, A. J., and B. J. Hoskins, 1978: The life cycles of some nonlinear baroclinic waves. *J. Atmos. Sci.*, **35**, 414–432, doi:10.1175/1520-0469(1978)035<0414:TLCOSN>2.0.CO;2.

Simpson, I. R., M. Blackburn, and J. D. Haigh, 2012: A mechanism for the effect of tropospheric jet structure on the annular mode–like response to stratospheric forcing. *J. Atmos. Sci.*, **69**, 2152–2170, doi:10.1175/JAS-D-11-0188.1.

——, T. G. Shepherd, P. Hitchcock, and J. F. Scinocca, 2013: Southern annular mode dynamics in observations and models. Part II: Eddy feedbacks. *J. Climate*, **26**, 5220–5241, doi:10.1175/JCLI-D-12-00495.1.

Son, S.-W., and S. Lee, 2006: Preferred modes of variability and their relationship with climate change. *J. Climate*, **19**, 2063–2075, doi:10.1175/JCLI3705.1.

——, N. F. Tandon, L. M. Polvani, and D. W. Waugh, 2009: Ozone hole and Southern Hemisphere climate change. *Geophys. Res. Lett.*, **36**, L15705, doi:10.1029/2009GL038671.

Strong, C., and G. Magnusdottir, 2008: Tropospheric Rossby wave breaking and the NAO/NAM. *J. Atmos. Sci.*, **65**, 2861–2876, doi:10.1175/2008JAS2632.1.

Sun, L., G. Chen, and J. Lu, 2013: Sensitivities and mechanisms of the zonal mean atmospheric circulation response to tropical warming. *J. Atmos. Sci.*, **70**, 2487–2504, doi:10.1175/JAS-D-12-0298.1.

Swart, N. C., and J. C. Fyfe, 2011: Ocean carbon uptake and storage influenced by wind bias in global climate models. *Nat. Climate Change*, **2**, 47–52, doi:10.1038/nclimate1289.

——, and ——, 2012: Observed and simulated changes in the Southern Hemisphere surface westerly wind-stress. *Geophys. Res. Lett.*, **39**, 16711, doi:10.1029/2012GL052810.

Thompson, D. W. J., and J. M. Wallace, 2000: Annular modes in the extratropical circulation. Part I: Month-to-month variability.

J. Climate, **13**, 1000–1016, doi:10.1175/1520-0442(2000)013<1000:AMITEC>2.0.CO;2.

Vallis, G. K., 2006: *Atmospheric and Oceanic Fluid Dynamics: Fundamentals and Large-Scale Circulation.* Cambridge University Press, 745 pp.

——, E. P. Gerber, P. J. Kushner, and B. A. Cash, 2004: A mechanism and simple dynamical model of the North Atlantic Oscillation and annular modes. *J. Atmos. Sci.*, **61**, 264–280, doi:10.1175/1520-0469(2004)061<0264:AMASDM>2.0.CO;2.

Woollings, T. J., and B. J. Hoskins, 2008: Simultaneous Atlantic–Pacific blocking and the northern annular mode. *Quart. J. Roy. Meteor. Soc.*, **134**, 1635–1646, doi:10.1002/qj.310.

——, A. Hannachi, B. J. Hoskins, and A. Turner, 2010: A regime view of the North Atlantic Oscillation and its response to anthropogenic forcing. *J. Climate*, **23**, 1291–1307, doi:10.1175/2009JCLI3087.1.

Xia, X., and E. K. M. Chang, 2014: Diabatic damping of zonal index variations. *J. Atmos. Sci.*, **71**, 3090–3105, doi:10.1175/JAS-D-13-0292.1.

Zhang, Y., X.-Q. Yang, Y. Nie, and G. Chen, 2012: Annular mode–like variation in a multilayer quasigeostrophic model. *J. Atmos. Sci.*, **69**, 2940–2958, doi:10.1175/JAS-D-11-0214.1.

Zurita-Gotor, P., J. Blanco-Fuentes, and E. P. Gerber, 2014: The impact of baroclinic eddy feedback on the persistence of jet variability in the two-layer model. *J. Atmos. Sci.*, **71**, 410–429, doi:10.1175/JAS-D-13-0102.1.